Neuroinflammatory and neurometabolic consequences from inhaled 2020 California wildfire smoke-derived particulate matter at a remote location

David Scieszka
University of New Mexico Health Sciences Center https://orcid.org/0000-0001-9357-7121
Russell Hunter
University of New Mexico Health Sciences Center
Jessica Begay
University of New Mexico Health Sciences Center
Marsha Bitsui
University of New Mexico Health Sciences Center
Yan Lin
University of New Mexico
Joseph Galewsky
University of New Mexico
Masako Morishita
Michigan State University
Zachary Klaver
Michigan State University
James Wagner
Michigan State University
Jack Harkema
Michigan State University
Guy Herbert
University of New Mexico Health Sciences Center
Selita Lucas
University of New Mexico Health Sciences Center
Charlotte McVeigh
University of New Mexico Health Sciences Center
Alicia Bolt
University of New Mexico Health Sciences Center
Barry Bleske
University of New Mexico Health Sciences Center

Christopher Canal
Virginia Commonwealth University
Ekaterina Mostovenko
Virginia Commonwealth University
Andrew Ottens
Virginia Commonwealth University
Haiwei Gu
Arizona State University
Matthew Campen (mcampen@salud.unm.edu)
University of New Mexico Health Sciences Center https://orcid.org/0000-0002-2292-5050
Shahani Noor
University of New Mexico Health Sciences Center

Article

Keywords: Neuroinflammation, inflammaging, microglia, VCAM-1, neurovascular unit, peripheral leukocytes, particulate matter, smoke, neurodegeneration

Posted Date: July 29th, 2021

DOI: https://doi.org/10.21203/rs.3.rs-722777/v1

Neuroinflammatory and neurometabolic consequences from inhaled 2020 California wildfire smoke-derived particulate matter at a remote location.

David Scieszka[1], Russell Hunter[1], Jessica Begay[1], Marsha Bitsui[1], Yan Lin[2], Joseph Galewsky[3], Masako Morishita[4], Zachary Klaver[4], James Wagner[5], Jack R. Harkema[5], Guy Herbert[1], Selita Lucas[1], Charlotte McVeigh[1], Alicia Bolt[1], Barry Bleske[6], Christopher G. Canal[7], Ekaterina Mostovenko[7], Andrew K. Ottens[7], Haiwei Gu[8], Matthew J. Campen[1*], Shahani Noor[9*]

[1] Department of Pharmaceutical Sciences, College of Pharmacy, University of New Mexico Health Sciences Center, Albuquerque, NM 87131

[2] Department of Geography and Environmental Studies, College of Arts and Sciences, University of New Mexico, Albuquerque, NM 87131

[3] Department of Earth and Planetary Sciences, College of Arts and Sciences, University of New Mexico, Albuquerque, NM 87131

[4] Department of Family Medicine, Michigan State University, East Lansing, MI 48824

[5] College of Veterinary Medicine, Michigan State University, East Lansing, MI

[6] Department of Pharmacy Practice and Administrative Sciences, College of Pharmacy, University of New Mexico Health Sciences Center, Albuquerque, NM 87131

[7] Department of Anatomy and Neurobiology, Virginia Commonwealth University, PO Box 980709, Richmond, VA 23298

[8] Arizona State University, Phoenix, AZ

[9] Department of Neurosciences, School of Medicine, University of New Mexico Health Sciences Center, Albuquerque, NM 87131

* Co-corresponding Authors:

- Matthew J Campen, PhD, Department of Pharmaceutical Sciences, MSC09 5360, 1 University of New Mexico, Albuquerque, NM 87131-0001, (505) 272-5569, MCampen@salud.unm.edu
- Shahani Noor, PhD, Neurosciences Department, School of Medicine, (505) 272-4411, snoor@salud.unm.edu,

Running title: Neuroinflammatory impact of wildfire smoke

Keywords: Neuroinflammation, inflammaging, microglia, VCAM-1, neurovascular unit, peripheral leukocytes, particulate matter, smoke, neurodegeneration

ABSTRACT

Utilizing a mobile laboratory located >300 km away from wildfire smoke (WFS) sources, this study examined the systemic immune response profile, with a focus on neuroinflammatory and neurometabolic consequences, resulting from inhalation exposure to naturally occurring wildfires in California and Arizona in 2020. After a 20-day exposure period, WFS-derived particulate matter inhalation resulted in significant neuroinflammation while immune activity in the peripheral (lung, bone marrow) appeared to be resolved in C57BL/6 mice. Importantly, WFS exposure increased cerebrovascular endothelial cell activation and expression of adhesion molecules (VCAM-1 and ICAM-1) in addition to increased glial activation and peripheral immune cell infiltration into the brain. Flow cytometry analysis revealed proinflammatory phenotypes of microglia and peripheral immune subsets in the brain of WFS-exposed mice. Interestingly, endothelial cell neuroimmune activity was differentially associated with levels of PECAM-1 expression, suggesting that subsets of cerebrovascular endothelial cells were transitioning to resolution of inflammation following the 20-day exposure. Neurometabolites related to protection against aging, such as NAD^+ and taurine, were decreased by WFS exposure. Additionally, increased pathological amyloid-beta protein accumulation, a hallmark of neurodegeneration, was observed. Neuroinflammation, together with decreased levels of key neurometabolites, have important implications in priming inflammaging and aging-related neurodegenerative phenotypes.

INTRODUCTION

Wildfire smoke (WFS) exposure poses an increasing threat to a growing and aging global population. A demonstrable increase in the extent of wildfires and resultant damage has been documented in the United States over the past 15 years, an effect which correlates well with changing global temperatures.[1] In 2020, wildfires from the west coast generated smoke that engulfed much of the United States in high concentrations of particulate matter (PM), potentially impacting the health and well-being of 100's of millions of citizens for several months.

Wildfires release high concentrations of airborne particulates and gases derived from varying biomass and anthropogenic fuels (*e.g.,* buildings, vehicles, etc) that create unfamiliar and toxic exposures to populations far away from the source. Both PM and carbon monoxide are stable components of WFS that can travel thousands of miles. Even at a distance, WFS exposures increase acute respiratory hospital admissions.[2, 3, 4, 5] Additionally, underserved minority populations, including Native American communities, are disproportionately vulnerable to wildfire events.[6]

Wildfires produce complex mixtures of inhaled toxicants that can not only damage the lungs but also promote systemic health effects. While most gaseous products remain localized, PM from WFS is carried far distances across the continent by prevailing winds. Short- and long-term pulmonary, cardiovascular, and neurological outcomes from inhaled ambient PM are well studied; however, relatively little is known about the impact of WFS-derived PM on neurological outcomes — including implications for priming age-related disease sequelae. Ambient $PM_{2.5}$ (PM less than 2.5 microns in aerodynamic diameter) has been associated with increased incidence of Alzheimer's disease and related disorders (ADRD), suicide, depression, psychosis, and other adverse neurological outcomes[7, 8, 9, 10]. Impairment of blood brain barrier (BBB) and neuroinflammation has been implicated in pathophysiology of these neurological disorders. More recently, neurometabolite alterations in relation to neuroinflammation are being recognized as key drivers underlying cellular senescence and neurodegenerative disorders[11, 12, 13].

Prior studies suggest that inhaled PM induces proteolytic activity in the lung, leading to shedding of endogenous peptide fragments into the circulation that are bioactive and promote systemic endothelial inflammatory responses[14, 15, 16]. The BBB consists of tightly connected brain endothelial cells contouring the vasculature of the CNS, with astrocytic end feet surrounding this vasculature, and nearby microglia capable of monitoring local events. Trafficking of leukocytes is heavily regulated by the BBB[17]. The serum-borne, endogenously released peptides from inhalant toxicants are thought to act through ligand-receptor endothelial interactions to upregulate adhesion molecules such as intercellular adhesion molecule (ICAM)-1 and the leukocyte chemoattractant CCL2 that may facilitate peripheral leukocyte transmigration into the CNS. CCL2 signaling activates the transmembrane adhesion molecule, leukocyte function-associated antigen-1 (LFA-1) on peripheral immune cells allowing them to interact with endothelial ICAM-1. Similarly, endothelial vascular cell adhesion molecule (VCAM)-1 interactions may play critical roles in regulating peripheral immune access to the CNS, and also mediating neuroinflammatory consequences of aging-related proteins in blood[18]. Endothelial cell activation and interaction with peripheral leukocytes may therefore initiate the neuroinflammatory events following environmental exposures, such as WFS, leading to reactive astrogliosis, inflammation, and neurodegenerative phenotypes.

The present study exploited naturally-occurring wildfires in California and Arizona in October of 2020 to examine the neuroinflammatory consequences of WFS-derived PM at a site >1000 km away from the source. PM concentrations used in this study, due to the distant site and dilution factor, reflect a level lower than that experienced by tens of millions of people living in California, Oregon, and Washington during these wildfire events in 2020. Hallmarks of aging- and ADRD-related neurodegeneration, such as metabolite alterations, microglial activation, and pathological β-amyloid accumulation, were examined to gather supportive evidence as to the *in vivo* relevance of WFS exposure as an unrecognized contributor to neurological aging and degenerative sequelae.

METHODS

***Animals and Exposures*.** Male C57BL/6 mice (Jackson Labs) at 2 months of age were housed in quarantine for one week prior to transport to the mobile laboratory (Figure 1A) located in Paguate, NM (35°08'07.7"N 107°22'34.4"W; Figure 1A). Mice were housed in AAALAC-approved facilities, on a 12h light:dark cycle and provided a standard chow diet and water ad libitum. Mice were transported to the mobile laboratory 3-days prior to exposure initiation so that they could be acclimated to the chamber conditions. A total of 24 mice were used, evenly divided into Filtered Air (FA) control and concentrated $PM_{2.5}$ exposed groups. All procedures were conducted with approval by the University of New Mexico Animal Care and Use Committee.

Exposures in the mobile laboratory were conducted in Hinners chambers with wire-bottom mouse cages; water was available to mice throughout the exposures, but food was withheld (4h/d). $PM_{2.5}$ concentration was facilitated by a Harvard-type concentrator and mice were exposed whole-body for 4 h per day for 20 consecutive days[19]. Exposures began on October 6, 2020, and the final day was October 25, 2020. After the last round of exposures, mice were transported back to the UNM laboratories and euthanized the following day for tissue collection.

Particulate Matter Characterization. Exposure concentrations were measured in real-time with a DustTrak II (TSI, Inc; Shoreview, Minnesota), and 47 mm quartz filter weights collected for the duration of each daily exposure were used to gravimetrically confirm final daily averages. Filter samples were processed and analyzed in Class 100 clean rooms at the Michigan State University Exposure Science Laboratory. The samples were analyzed gravimetrically for particle mass using a microbalance (XPR6UD5, Mettler Toledo) in a temperature- and humidity-controlled clean laboratory as described in the Federal Reference Method [20]. PM samples collected on quartz filters were maintained at -40°C after sampling and were analyzed for carbonaceous aerosols (organic carbon and elemental carbon) by a thermal-optical analyzer (Sunset Laboratory) using the NIOSH 5040 method.

Particle samples collected on Teflon filters were wetted with ethanol and extracted in 1% nitric acid solution. The extraction solution was sonicated for 48 h in an ultrasonic bath, and then allowed to

passively acid-digest for two weeks. Extracts were then analyzed for twenty trace elements using high-resolution inductively coupled plasma-mass spectrometry (ELEMENT2, Thermo Finnigan). This analysis method incorporated daily quality assurance and quality control measures including field blanks, Type I water blanks, replicate analyses and external standards as described[21].

Quantification of levoglucosan was performed in the MSU Mass Spectrometry and Metabolomics Core. The details of sample extraction and analysis are described elsewhere [22]. In brief, for each sample, PM from approximately 100 mg of filter punches was extracted with 3 mL methanol containing 2 $\mu g \cdot mL^{-1}$ sedoheptulose anhydride as an internal standard (Millipore Sigma). One milliliter of the methanolic extract was dried down and derivatized with 100 µL of N-trimethylsilylimidazole (Millipore Sigma). One milliliter of the derivatized samples in splitless mode was analyzed using an Agilent 7890A GC/single quadrupole mass spectrometer with 5975C inert XL MSD. The mass spectrometer was operated using 70 eV electron ionization in selected ion monitoring mode for m/z 204 and 333. Quantification of levoglucosan, 3TMS derivative were based on a levoglucosan (Millipore Sigma) standard curve.

Lung Lavage, Cytokines, and Histopathology*.* Following euthanasia, lungs were lavaged with phosphate buffered saline as previously described. Total cell counts and differentials were conducted in a blinded manner. Cytokines were measured in BALF using an electrochemiluminescent assay (MesoScale Discovery, V-PLEX Proinflammatory Panel 1 and Cytokine Panel 1 Mouse Kits), according to manufacturer's instructions. Lungs were either perfusion fixed at 25 cmH_2O in 4% paraformaldehyde for histology (N=6/group) or frozen in liquid nitrogen. Transverse-oriented serial sections, 2-3 mm, were excised from the fixed left lung lobe, embedded in paraffin, and 5-6 µm thick sections cut from the anterior surface. Lung sections were stained with hematoxylin and eosin (H&E) for light microscopic examination by a board-certified veterinary pathologist (JRH) to determine exposure-related changes.

Echocardiography*.* Before transport to the mobile exposure laboratory and after exposures just prior to euthanasia, mice were briefly anesthetized with isoflurane for doppler ultrasound assessment of cardiac function (Vevo LAZR, FUJIFILM VisualSonics). Anesthesia was maintained at a light level,

targeting heart rate values above 400 beats per minute. Short-axis M-mode images were collected on all mice for assessment of cardiac output, ejection fraction, end-systolic dimensions and end-diastolic dimensions.

***Brain tissue digestion for flow cytometry*.** Under isoflurane anesthesia, mice underwent transcardial ice-cold 0.1M PBS (pH=7.4) perfusion. One brain hemisphere was harvested in ice-cold HBSS buffer and processed immediately according to Miltenyi gentleMACS^{TM} adult neural tissue digestion protocol, as described[23]. Briefly, brain tissues were minced with fine tip scissors and processed with enzymatic and mechanical digestion steps with gentleMACS ^{TM} Octo dissociator with heaters (Miltenyi Biotec, CA, USA). Following digestion steps, cell suspensions were passed through 70um cell strainers. Myelin debris were removed with Debris removal solution, used according to the manufacturer's protocol. Cells were resuspended in PBS (without calcium and magnesium, Sigma-Aldrich, St. Louis, MO) and kept on ice until proceeding to viability dye staining.

***Cell staining for surface and intracellular antigens for flow cytometry*.** For flow cytometry analysis, live cells were counted on a hemocytometer using trypan blue staining exclusion criteria. Between 0.2-1x10^6 cells were transferred in flow assisted cell sorting (FACs) tubes, stained with Viability dye eFlour 450 (eBioscience, San Diego, CA) for 30 mins. After a wash with FACs buffer (1x PBS containing 0.5% bovine serum albumin and 1mM EDTA) and incubation with a saturating solution of Fc block (BD Biosciences, San Jose, CA, USA), cells were stained for fluorochrome-conjugated antibodies for surface antigens for 25 min in the dark on ice. Antibodies against mouse CD11b, CD45, MHC-II, CD31 were all purchased from Themo Fisher Scientific, MA, USA and were used as 0.125-0.5µg/10^6 cells, as recommended by the manufacturer. Cells were examined for intracellular levels of various proinflammatory factors- tumor necrosis factor, TNFα, CCL2 and inducible nitric oxide synthase, iNOS. For intracellular staining, cells were fixed with Fixation buffer and then permeabilized using intracelullar fixation and permeabilization buffer set (eBioscience, USA). Cells were then stained with fluorochrome-conjugated antibodies for the intracellular immune factors for another 1 h at room temperature in the

dark. After another wash with 1x permeabilization buffer, cells were resuspended in 250-300µl FACs buffer and immediately proceeded for data acquisition. At least 50,000 live cell events were collected for each sample. Single-stained controls and isotype controls were used for laser compensation and data analysis. Data were acquired using the BD LSR Fortessa cell analyzer (BD Biosciences, San Jose, CA) and analyzed using Flow Jo software v10.7.1.

Flow cytometry gating strategy. The gating strategy for determining different cell subsets in the brain tissues is similar described in our prior report [23]. Briefly, doublets (cell clumps) were excluded, and the live cells were identified based on their size, granularity (FSC v SSC) and negative viability dye staining**.** Cerebrovascular endothelial cells were identified based on negative expression of the common leukocyte marker, CD45 and positive staining for CD31 (PECAM-1, Platelet endothelial cell adhesion molecule-1). All $CD45^+$ cells were first gated for PMN or neutrophil marker, Ly6G (1A8) staining, which were also verified by their positive CD11b staining. The population of $CD45^+1A8^-$ (leukocytes that are not neutrophils) were further analyzed to identify microglia with low or medium expression of CD45 ($CD45^{low/med}$, CD11b+) as distinguished from infiltrating macrophages/monocytes with $CD45^{high}$ expression ($CD45^{high}$ CD11b+). Additionally, infiltrating monocytes/macrophages were further analyzed for Ly6C expression to identify inflammatory monocytes ($1A8^-CD11b^+CD45^{high}Ly6C^+$). Median or geometric mean fluorescent intensities were plotted for activation markers or cytokine expression on these different immune and endothelial cell subsets.

Metabolomics tissue preparation. Briefly, each cerebellum sample (~20 mg) was homogenized in 200 µL MeOH:PBS (4:1, v:v, containing 1,810.5 µM $^{13}C_3$-lactate and 142 µM $^{13}C_5$-glutamic Acid) in an Eppendorf tube using a Bullet Blender homogenizer (Next Advance, Averill Park, NY). Then 800 µL MeOH:PBS (4:1, v:v, containing 1,810.5 µM $^{13}C_3$-lactate and 142 µM $^{13}C_5$-glutamic Acid) was added and, after vortexing for 10 s, the samples were stored at -20°C for 30 min. The samples were then sonicated in an ice bath for 30 min. The samples were centrifuged at 14,000 RPM for 10 min (4°C), and 800 µL of supernatant was transferred to a new Eppendorf tube. The samples were then dried under

vacuum using a CentriVap Concentrator (Labconco, Fort Scott, KS). Prior to mass spectrometry analysis, the obtained residue was reconstituted in 150 µL 40% PBS/60% ACN. A quality control sample was pooled from all the study samples.

Liquid Chromatography–Tandem Mass Spectrometry (LC–MS/MS). Targeted LC-MS/MS techniques were similar to several recent reports[24, 25, 26, 27, 28, 29]. Briefly, LC-MS/MS experiments were performed on an Agilent 1290 UPLC-6490 QQQ-MS (Santa Clara, CA) system. Each cerebellum sample was injected twice: first a 10 µL volume for analysis using negative ionization mode and second a 4 µL volume for analysis using positive ionization mode. Both chromatographic separations were performed in hydrophilic interaction chromatography (HILIC) mode on a Waters XBridge BEH Amide column (150 x 2.1 mm, 2.5 µm particle size, Waters Corporation, Milford, MA). The flow rate was 0.3 mL/min, auto-sampler temperature was kept at 4ºC, and the column compartment was set at 40ºC. The mobile phase was composed of Solvents A (10 mM ammonium acetate, 10 mM ammonium hydroxide in 95% H_2O/5% acetonitrile) and B (10 mM ammonium acetate, 10 mM ammonium hydroxide in 95% acetonitrile/5% H_2O). After the initial 1 min isocratic elution of 90% B, the percentage of Solvent B decreased to 40% at t=11 min. The composition of Solvent B maintained at 40% for 4 min (t=15 min), and then the percentage of B gradually went back to 90%, to prepare for the next injection.

The mass spectrometer is equipped with an electrospray ionization (ESI) source. Targeted data acquisition was performed in multiple-reaction-monitoring (MRM) mode. The whole LC-MS system was controlled by Agilent Masshunter Workstation software (Santa Clara, CA). The extracted MRM peaks were integrated using Agilent MassHunter Quantitative Data Analysis (Santa Clara, CA). Acetonitrile (ACN), methanol (MeOH), ammonium acetate, and acetic acid, all LC-MS grade, were purchased from Fisher Scientific (Pittsburgh, PA). Ammonium hydroxide was bought from Sigma-Aldrich (Saint Louis, MO). Standard compounds corresponding to the measured metabolites were purchased from Sigma-Aldrich and Fisher Scientific.

Immunofluorescence Microscopy. The right-hemisphere of each fresh-frozen mouse brain was cryosectioned (10 μm thick) along the sagittal plan starting 1.5 mm from the lateral aspect. Brains from APP/PS1 mice (Jackson Labs) with mutant human amyloid precursor protein and presenilin 1 on a C57BL/6 background were used as a positive control for amyloid pathology. Sections were collected on charged slides, air dried and then fixed with 4% paraformaldehyde. Sections were blocked and permeabilized in 5% normal goat serum and 0.1% Triton X-100 for 1 h at room temperature. Sections were then probed at 4 °C overnight with primary antibodies in blocking buffer: vascular marker anti-rat zonula occludens 1 (ZO1, Developmental Studies Hybridoma Bank, Iowa City, IA; R26.4C, 1:5), astrocytic marker anti-chicken glial fibrillary acidic protein (GFAP, Abcam, Cambridge, MA; ab4674, 1:2500), amyloid pathology marker anti-mouse Aβ-42 (Thermo Scientific, MA5-36246, 1:500), early neurodegenerative disease marker anti-rabbit Sorcin (Thermo Scientific, PA5-95611, 1:500), microglial marker anti-guinea pig ionizing calcium binding adaptor molecule 1 (IBA1, Synaptic Systems, Goettingen, Germany; 234-004, 1:2000), BBB permeation marker anti-rabbit albumin (Bioss, bs-2256R, 1:300). Sections were then probed with corresponding AlexaFluor 488/568/680/750-conjugated goat secondary antibodies at room temperature for 2 h. Mounted sections were cover-slipped in ProLong Diamond Antifade Mountant (Thermo Scientific). Slides were imaged using constant exposure and illumination settings optimized per channel via multichannel immunofluorescence with a Zeiss AxioImager M2 microscope with structured illumination and optical sectioning (0.5-μm stack thickness). Image acquisition and visualization were performed with Zeiss Zen 2.1 software with constant gray level settings per channel across all sections.

Amyloid beta 42 ELISA. Soluble toxic Aβ-42 was assessed in brain tissue samples via ELISA with the Human/rat β-amyloid (Aβ-42) ELISA kit (Wako Pure Chemical Industries, 290-62601, Richmond, VA), according to the manufacturer's instructions. Total sample protein was acquired by performing a BCA with the Pierce™ BCA Protein Assay Kit (Thermo Scientific, 23225). Resultant Aβ peptide content was normalized to total sample protein content.

Statistics. In the event of normally distributed data, student's t-test was used. For non-normally distributed data, t-tests were employed on Log_2 transformed data. Pearson's correlation was performed on PM elemental composition. Tests were either conducted in GraphPad Prism v9.1.1 or Rstudio v1.4.1564.

RESULTS

Exposure Characterization: The mobile laboratory-based concentration of $PM_{2.5}$ led to 4-h exposure levels averaging 104 $\mu g/m^3$ across the 20-d period (Figure 1B). During the peak of wildfire smoke transported to this region, high concentrations of 209 and 191 $\mu g/m^3$ were seen (first 2 days of exposure). We also measured the overall content of levoglucosan, a specific marker for woodsmoke, in pooled PM filter samples, which revealed that the first three days of exposure had a high contribution of wood burning in the $PM_{2.5}$. Increased levoglucosan levels were also evident on exposure days 13-16. Potassium levels in the WFS appeared elevated on days with greater wildfire contributions (Table S1) and correlations among K, Mg, and Mn were noted, consistent with previous studies of wildfire PM composition (Figure S1)[30]. Modeling of wind trajectories for the initial period of the exposure identified a strong likelihood that woodburning-derived PM originated in southern California (Figure 1C). Geospatial analysis of the western US revealed extensive smoke distribution during the exposure period. Additional contributing wildfires were present in Colorado and Arizona. Importantly, mice were only exposed for four hours a day, so that the 24 h average $PM_{2.5}$ exposure could be estimated as much lower, potentially <20 $\mu g/m^3$ (Table S1).

Pulmonary and Systemic Responses: Histological assessment of lungs revealed a modest increase in the macrophage population in WFS-exposed mice compared to FA (Figure 2A,B). This was confirmed quantitatively with cells recovered in the BALF increased four-fold in WFS- versus FA-exposed mice, principally due to macrophage elevations (Figure 2C). The numbers of neutrophils were not elevated by WFS exposure (Table S2). However, neutrophil recruitment cytokines IL-17, MIP1, and MIP2 were statistically elevated (Figure 2D), while TNFα and other conventional inflammatory

mediators were unaltered (Table S2). The absence of neutrophils suggests that any acute pulmonary inflammatory phase had subsided, with effector responses trending downward towards resolution. Additionally, the inflammatory cytokine IP10 was significantly elevated, indicating a persistent response in cellular subtypes of monocytes, T cells, NK cells, or eosinophils[31]. We questioned whether this inflammation was reflected systemically through bone marrow examinations. Interestingly, MIP2 and IP10 were elevated in the bone marrow of WFS-exposed mice (Figure 2E). However, many other BALF, whole lung, regional brain tissue, and bone marrow inflammatory protein markers were unaltered by the 20-day WFS exposure (Tables S2-S5), including KC/Gro, TNFα, and IL-6, confirming that the overall pulmonary inflammatory response to this exposure was expectedly modest, or resolving from the earlier higher exposure concentrations. Additionally, echocardiography was performed to assess cardiac function; however, no significant changes were noted between FA and WFS mice after the 20-d exposure (Table S6)

Neuroinflammaging: We assayed prefrontal cortices and hippocampal regions for inflammatory proteins and cerebelli for aqueous metabolites including specific assessments for NAD and related metabolites. Cytokines from the hippocampus showed no statistical differences (Table S4). However, prefrontal cortices showed a decrease in KC/Gro (Table S4). WFS-exposed mice displayed reduced NAD+, NADH, succinate, and taurine compared to FA-exposed mice (Figure 3A), all of which have important implications for aging[12, 13, 32]. These aging-related metabolites prompted a direct examination of Aβ-42 levels, the more pathogenic peptide variant that aggregates faster, which was significantly increased in WFS-exposed mouse brain (Figure 3A). Localization of increased Aβ-42 appeared proximal to cerebrovasculature together with greater staining for the early neurodegenerative disease marker sorcin[33] as also found in matched staining of APP/PS1 model mouse brain (Figure 3C). Taken together, WFS exposure – from a source >1,000km away – gives rise to numerous markers of an accelerated inflammaging response with increased markers consistent with a neurodegenerative phenotype.

Given the proximity of these markers to the cerebrovasculature, we further wanted to assess indications of a neuroinflammatory response comparable to outcomes we have seen with other inhaled toxicant exposures[14, 15, 23]. Phenotypically, the neurovascular unit appeared similar to that previously seen after pulmonary particulate exposure, with extravascular albumin staining, increased GFAP process volume and greater IBA1 localization to indicate a reactive, neuroinflammatory state in WFS-exposed mice (Figure 4A). A neuroinflammatory state was affirmed with cytometric quantitation of microglia and CNS infiltrating peripheral immune cells (Supplemental Figure 2: gating strategy). An increase of microglial frequency along with their surface expression of CD45 were significantly elevated in WFS-exposed brains compared to FA controls (Figure 4B). Moreover, intracellular levels of proinflammatory proteins CCL2 and iNOS were increased in microglia after WFS-exposure (Figure 4B). We validated microglial activation by measuring elevated surface expression of ICAM-1 and iNOS, though the increasing trend in TNFα expression did not reach significance (Figure 4B).

Given peripheral immune reactivity (Figure 2C), infiltration of peripheral immune cells into the CNS was also examined by cytometric analysis of the perfused brains. Contrary to the BALF, an increased influx of mature ($1A8^{high}$) neutrophils was detected in WFS-exposed brains, displaying significantly higher levels of CD11b and MHC-II expression (Figure 5A). The marker $CD45^{high}$ includes various subsets of peripheral leukocytes, and no changes were observed on this macro level. However, further analysis of a $CD45^{high}Cd11b^{+}$ subset revealed significant increases in CNS-infiltrating $Ly6C^{+}$ inflammatory monocytes in the brain, suggesting an influx of these cells due to WFS exposure (Figure 5B). Furthermore, there were significant increases in $CD45^{high}$LFA-1^{+} and $CD45^{high}$ICAM-1^{+} peripheral macrophages that exhibited a greater expression of MHC-II in WFS-exposed brains (Figure 5C).

Flow cytometry also revealed a complex phenotype among brain endothelial cells ($CD31^{+}/CD45^{-}$) following 20-d WFS exposure, with subpopulations divided by their level of CD31 expression (Figure 6A). WFS shifted $CD31^{+}/CD45^{-}$ endothelial cells overall to a greater expression of CD31 (Figure 6) consistent with vascular repair and restoration of the BBB,[34] with these pro-repair $CD31^{high}/CD45^{-}$ cells

expressing exhibiting reduced levels in most inflammatory markers (Figure 6C). At the same time, $CD31^{med}/CD45^{-}$ cells retained their inflammatory profile after WFS exposure with increases in CCL2, TNFα, iNOS, LFA-1 and VCAM-1 (Figure 6B).

DISCUSSION

The recent spate of wildfires around the globe have provoked concern that smoke exposures may promote vascular and, by extension, neurological consequences [35, 36]. While clear relationships between ambient air pollutants, such as $PM_{2.5}$ and carbon monoxide, and increased incidence of ADRD have been reported[7, 8, 9], there have been no specific assessments of wildfire smoke PM impacts on neuroinflammation or markers of ADRD. Findings of the present study confirm that the WFS-derived $PM_{2.5}$ traveling from distant wildfires can promote numerous outcomes consistent with ADRD pathogenesis and neurological aging.

Neuroinflammation and key reduced metabolites occurred in otherwise healthy mice exposed for 80 total hours of WFS-derived $PM_{2.5}$, including microglial activation and peripheral leukocyte invasion. The concentrations in our study averaged 104 $\mu g/m^3$ for only 4 h/d of exposure. Findings of a 13-day wildfire episode in Washington state found 24 h average $PM_{2.5}$ to be 96 $\mu g/m^3$ (up from a baseline of 4.3 $\mu g/m^3$) with two counties experiencing peak concentrations near 400 $\mu g/m^3$ [37, 38]. During this period, we estimate that over 1.6 million residents of Washington state experienced 24 h exposures well in excess of 100 $\mu g/m^3$ on average, and all 7 million people in the state were exposed to levels higher than our 24 h exposure average (Figure S3). Similar exposures were seen for populations in Oregon and California. In addition to PM, carbon monoxide and potentially other gaseous pollutants can further contribute to neurological morbidity [39]. Notably, the long distance from the source and method of $PM_{2.5}$ fractionation used in our study would lead to disproportionately low gaseous pollutants; thus, this study does not address potential additivity of the total pollutant atmosphere.

The pathways leading from inhaled pollutants to neurological outcomes are being discerned through mechanistic toxicological studies. We have suggested that circulating bioactive peptide fragments arise

from pulmonary matrix metalloproteinase activity following inhalation of a diverse array of pollutants, including PM and ozone [14, 23, 40, 41]. Endothelial VCAM-1 drives leukocyte invasion, which reduces BBB integrity and reactive consequences at the neurovascular unit; specific aging-related circulating factors may augment VCAM-1 signaling and promote BBB impairment [18]. Controlled exposures to woodsmoke caused a circulating bioactivity that induced endothelial VCAM-1 in *ex vivo* incubations, notably more potently than other emissions including diesel/gasoline emissions and ozone.[42] The present findings from flow cytometric assessment of VCAM-1 expression in $CD31^{med}/CD45^{-}$ cerebrovascular endothelial cells confirms the *in vivo* relevance of this effect, but notably at a remarkably low concentration of $PM_{2.5}$. Identification of evoked circulating factors after wildfire smoke exposure and the endothelial receptor interactions is essential to understanding pathways that confer susceptibility among individuals. Furthermore, the apparent initial steps of BBB repair and inflammation resolution, seen as an increase in $CD31^{high}/CD45^{-}$ cells with reduced iNOS, CCL2, and TNFα expression after 20d of exposure, highlight another potential contributor to susceptibility, with genetic and lifestyle factors in the general population adding variability to the efficiency and quality of inflammatory resolution.

Endothelial cell responses are complex, with control and PM-exposed mice exhibiting relatively different levels of CD31, which drove the segregated analysis of $CD31^{med}$ versus $CD31^{high}$. CD31 is not a passive, constitutive marker of endothelial cells in the brain, and it has been noted as a key player for maintaining BBB integrity[34] and neutrophil recruitment in inflamed brains[43]. Using a bifurcated analysis strategy for the endothelial cell analysis, we illustrate a potentially dynamic system that is crucial to acclimation to environmental stressors. Cells highly expressing CD31 were also downregulating other canonical inflammatory pathways, including CCL2 and iNOS. Thus, we postulate that subchronic exposure to inhaled PM from WFS likely leads to repair of the cerebrovascular endothelium, but little can be inferred from the present study design as to the timeframe of this resolution.

Despite the worst concentrations of the exposure occurring on the first two days of the 20-d exposure, there was little indication of resolution of microglial activation or the invading peripheral leukocytes.

Peripheral immune cells were not only in greater numbers in the brains of WFS-exposed mice, but they also expressed greater MHC-II protein on the surface, which is associated with the inflammatory response in neurodegenerative diseases [44, 45]. Furthermore, peripheral immune cells expressed higher levels of inflammatory markers ICAM-1, iNOS, and CCL2 in WFS-exposed mice. These proinflammatory immune cells may interact with microglia and astrocytes and further propagate neuroinflammation. Eventually these immune cells may help resolve inflammation or injury in the brain, but the resolution of this infiltration may require months [46]. Repeated insults may therefore confound beneficial outcomes or escalated other pathologies such as Alzheimer's disease or multiple sclerosis [46]. Understanding the molecular and cellular pathways regulating the resolution, as well as the range of environmental and pathological stressors that promote inflammation is, again, a priority for understanding how susceptibility to neurodegenerative disease arises.

Environmental stressors, including air pollution, have been associated with neurodegenerative diseases[9, 39, 47], and the present study details pathways that may be points of vulnerability for individuals with genetic predisposition for ADRD. Genetic heritability is actually quite variable across different syndromes of dementia. Frontotemporal dementia only has clear heritability evidence in up to 30% of cases, most of which can be explained by single gene mutations (*e.g.*, microtubule-associated protein tau and progranulin) [48]. Alzheimer's disease has a much higher heritable basis, between 60-80% [49]. Thus, environmental factors and other pathologies must account for a substantial portion of the remaining incidence. Furthermore, even with the highly heritable Alzheimer's disease, the age of onset may be influenced by environmental factors interactions[50]. The elevation of Aβ-42 seen after WFS in mice is reminiscent of previous studies of acute ozone inhalation[23]. Aβ-42 is an early pathogenic indicator with aggregating potential in humans, but the existence of rodent Aβ-42 in response to air pollution is unclear as mice do not naturally form plaques[51]. Aβ-42 may be elevated due to increased production or reduced clearance, possibly a repercussion from microglial diversion to the neurovascular unit. Regardless of the mechanism, impairing BBB, driving neuroinflammation and reducing key

metabolites may be central to environmental contributions to ADRD incidence; the sensitivity of individuals to these effects and the efficiency of resolution may influence susceptibility among individuals.

Compromised metabolism is a major hallmark of cellular aging. Neurons and neuro-supportive cells undergo numerous changes with aging including reductions of protein quality control and lysosomal dysfunction, along with DNA damage and epigenetic modifications. Genetic variants that influence neural longevity include FOXO3, IL-6, and TOMM40-APOE-APOC1.[52, 53, 54] However, it has been estimated that environmental contributions may account for as much as 70% of premature aging.[55] The aging neuron is vulnerable to reduced metabolic capacity, highlighted as a loss of nicotinamide adenine dinucleotide (NAD^+) concentrations.[56] This reduction in bioenergetics negatively impacts DNA repair, which appears central to a downward spiral of cellular functionality. NAD^+ levels can be augmented with precursor supplementation (nicotinamide mononucleotide) that reduces DNA damage and extends healthspan in mouse models.[57, 58] Following WFS exposure, however, we see significant reductions in NAD^+ levels, along with NADH, succinate, and taurine. While this trend does not indicate aging, per se, it at least suggests that WFS exposure may add to the burden of aging-related metabolic impairments in the brain. More importantly, neurometabolite alterations are associated with oxidative damage and chronic neuroinflammation [11, 32, 59]. NAD^+ and taurine boost anti-inflammatory activity. Reduced levels of NAD^+ and taurine are associated with chronic neuroinflammation and drives neuroinflammaging, a low-grade inflammation state that drives aging process [60, 61]. NAD^+ is involved in stress resistance and synaptic plasticity and is downregulated in aged animals, while the conversion of NAD^+ to NADH is important for ATP generation [11]. Succinate is important for mitochondrial function and oxidative metabolism [62]. Taurine has been shown to be neuroprotective during aging [63].

In summary, WFS exposure activated microglia, drove neural infiltration of inflammatory monocytes and MHC-II^+ cells, decrease neuroprotective metabolites, and increase Aβ-42 when examining the entire brain. Overall enhanced neuroinflammation from WFS exposure potentially contributes to neurological

aging and pathology, and the effects demonstrated at environmentally-relevant concentrations warrant further exploration into long-term neurological sequelae and vulnerability for specific subpopulations, especially in the young and those of advanced age. Beyond simple metrics of plaque buildup, we identified key components of ADRD promotion from systemic inflammation to cerebrovascular endothelial activation and glial proinflammatory activation to downregulation of key energetic metabolites. Based on our novel findings neuroimmune activity and neurometabolism, these data point to fundamental effects of exposure to WFS leading to wide ranging pathology that may contribute to aging process.

Acknowledgements: This study was funded by grants from the NIH (R01 ES026673, R01 ES014639, P42 ES025589). The authors are grateful to the support from the Paguate Village and Pueblo of Laguna communities, especially Greg Jojola, Pat Pruitt, Steven Etter, and Kyle Swimmer. The authors thank Dong Sun for access to APP/PS1 mouse brains. The antibody to ZO1 (R26.4C) was developed by D.A. Goodenough at Harvard Medical School, obtained from the Developmental Studies Hybridoma Bank, created by the Eunice Kennedy Shriver National Institute of Child Health and Human Development (NICHD) and maintained at the University of Iowa. Chris Shuey of the Southwest Research and Information Center was essential to engaging the community and siting the mobile laboratory.

Author contributions

Study was designed by MJC, JH, JW, MM, DS, SN, AB, AKO, and BB

Exposures and particulate collection were implemented by MJC, SL, JGB, MB, DS, BB, and RH

Particle measurement and characterization were implemented by MM and ZK

Data compilation and analysis were conducted by MJC, DS, JGB, and MM

Lung histopathology was conducted by JW and JH

Brain histopathology was conducted by AKO, EM and CGC

Metabolomics were conducted by HG

Flow cytometry was conducted by DS and SN

Cytokine and protein measurements were conducted by GH, DS, CM, and AB

Geospatial and meteorological analysis were conducted by JRG and YL

Principal writing of the manuscript was conducted by DS, MJC, SN, with major sections contributed by HG, MM, ZK, JG, AKO and YL.

All authors read and take responsibility for the entire manuscript.

Competing interests

The authors declare no competing interests with the results of this study and content of the manuscript.

Data Availability

Data are available upon request to the corresponding authors.

FIGURE LEGENDS

Figure 1. Exposure to concentrated WFS particulates in Paguate, NM. **A.** Mobile laboratory containing rodent exposure chambers and a Harvard-type particle concentrator. **B.** Daily $PM_{2.5}$ gravimetric mass concentrations for the 20 days of exposure (black dots), along with levoglucosan measures (red bars) that span 3-4 days, as filters were pooled to provide sufficient material. **C.** Smoke and wildfire locations for 3 representative days in October 2020 derived from the National Oceanic and Atmospheric Administration Hazard Mapping System (HMS) Fire and Smoke Product [64, 65, 66], with dashed lines indicating the link to exposures days in B. The black star indicates the location of the mobile laboratory in Paguate, NM. Smoke plumes shown in pink were derived manually from geostationary and polar-orbiting satellites and represent a minimum smoke PM2.5 concentration of 5 µg/m3. Fire locations shown by triangles were obtained with automated fire detection algorithms; the

nearest fire (on the border of Arizona and New Mexico) was over 300 km away from the mobile laboratory [65].

Figure 2. Significant pulmonary and bone marrow cytokine responses to 20-day exposure to wildfire smoke (WFS). Light photomicrographs of hematoxylin and eosin-stained lung tissue from the left lung lobe of mice exposed to **A)** filtered air or **B)** concentrated fine ambient particles. Slightly more alveolar macrophages (arrows) were present in WFS-exposed mice than filtered air control mice. Stippled arrow, particle laden-alveolar macrophage (black cytoplasmic material); Sold arrow, alveolar macrophage without cytoplasmic particles; a, alveolus; ad, alveolar duct. **C.** Airway macrophages in bronchoalveolar lavage fluid were significantly elevated after WFS exposure. **D.** Whole lung cytokine IL-17, and bronchoalveolar lavage cytokines, MIP-1a, MIP-2, and IP-10 were significantly elevated by WFS. **E.** Bone marrow concentrations of MIP-2 and IP-10 were elevated by WFS. n=6 or 10 independent samples; two-tailed t-test; mean and SEM shown, *p<0.05, **p<0.01, ***p<0.005, ****p<0.001. All measured cytokines are provided in Supplemental Tables 2-5.

Figure 3. Markers related to aging and neurodegenerative disease pathogenesis. A. NAD^+, NADH, succinate, and taurine were all downregulated and amyloid beta (Aβ) levels were upregulated in WFS-exposed mice. **B.** Representative images of neurodegenerative pathogenic markers found at the neocortical neurovascular unit in WFS-exposed mice. Brain Aβ-42 (red) increases in WFS-exposed mice were observed only proximal to the neurovascular unit (endothelial ZO1 and astrocyte GFAP). Additionally, the early pathogenic marker Sorcin increased (green), indicating ER stress / unfolded protein responses proximal to areas of Aβ-42 staining, which was also observed in unexposed APP/PS1 mice of the same age and background as a positive control, though they exhibited higher density Aβ-42 aggregation. N= 6 independent samples; two-tailed t-test; mean and SEM shown, $\log_2$ correction for normality.

Figure 4: Microglial activation following WFS. A. Imaging of the neurovascular unit reflected similar pathology as reported with other pollutants previously with more pronounced GFAP (cyan) staining and

a greater presence of IBA1^{+} (green) microglia/macrophages adjacent to large-diameter (> 20 μm) cerebrovasculature (ZO1^{+}, purple), along with an increased staining in parenchymal albumin (red) in WFS-exposed relative to filtered air control. **B.** Percentage of microglia and their surface expression levels of CD45, adhesion molecule ICAM-1 and intracellular levels of proinflammatory factors, iNOS, TNFα and CCL2 were analyzed. N=3-5 independent samples; two-tailed t-test; mean and SEM shown.

Figure 5: Infiltrating immune cells in the brain following WFS exposure. A. Increased frequency of mature neutrophils (with high expression of 1A8), along with overall increase in MHC2 and CD11b surface expression of all CD45^{+}1A8^{+} neutrophils in the brain due to WFS exposure. **B.** Inflammatory monocytes in the brain were increased in frequency with WFS exposure. **C.** CNS infiltrating CD45^{high}CD11b^{+} macrophage/monocyte population shows increased MHC2 expression and frequency of LFA-1+ and ICAM-1+ peripheral leukocytes were also increased due to WFS exposure. N=4-5 independent samples; two-tailed t-test; mean and SEM are shown.

Figure 6: Cerebrovascular endothelial cells exhibit a heterogeneous inflammatory response to WFS. A. Representative flow cytometry plots of endothelial cells (with medium and high expression of CD31/PECAM-1 on CD45^{-} cells) in the brain in FA or WFS exposure group. These two subsets of endothelial cells displayed comparatively different neuroimmune activity profile, as detailed in B-C. **B.** Frequency of endothelial cells with high expression of CD31 was increased following WFS exposure, however, these endothelial cells displayed reduced levels of these proinflammatory factors. Increased frequency of ICAM-1 expressing endothelial cells were observed due to WFS exposure in this endothelial subset despite no changes in MHC2. **C.** Frequency of CD31^{med} endothelial were reduced following WFS exposure, however, these cells displayed increased proinflammatory phenotype such as increased levels of CCL2, TNFα and iNOS, although reduced levels of ICAM-1 and MHC2 were observed. N=4-5 independent samples; two-tailed t-test; mean and SEM are shown.

Figure S1. Pearson's correlation analysis of elemental composition of PM2.5 across the 20 days of exposure. Asterisks indicate significant association ($p<0.05$). Clusters of elements that line up with

previous reports of wildfire composition, including potassium, magnesium, and manganese were noted, while days with lower wildfire smoke contribution exhibited clustering of crustal elements (iron, aluminum, rare earth metals) common to the rural southwestern United States.

Figure S2. Gating strategy for flow cytometry analysis. Representative flow cytometry plots demonstrate the grating strategy used for immune cell percentages or fluorescence intensities of various immune markers. Potential live cells were gated based on their light scatter properties, side scatter area (SSC-A) vs forward scatter-area (FSC-A), doublets (cell clumps) were excluded and live cells from "single cell" population were identified with the absence of viability dye staining. Live cells were then assessed on their CD45 (common leukocyte marker) expression. $CD45^-$ cells were analyzed for CD31 (PECAM) expression denoting endothelial cells. $CD45^+$cell population were first analyzed for Ly6G (1A8) expression denoting neutrophils. $CD45^+1A8^+$ were further analyzed to identify neutrophil population with $1A8^{high}$ expression. $CD45^+$1A8- population (leukocytes but not neutrophils) were further analyzed against CD11b expression to identify microglia $CD45^{med}$ $CD11b^+$ population, as compared to $CD45^{high}CD11b^+$ macrophage/monocytes population. Inflammatory monocytes were identified based on their $Ly6C^{high}$ expression ($CD45^+CD11b^+Ly6C^{high}$).

Figure S3. Reanalysis of data reported by Liu and colleagues[35,36] from September 2020 wildfires revealed over 1.6 million people in Washington state were exposed to concentrations in excess of 100 $\mu g/m^3$ for the 13-day period.

REFERENCES:

1. Reid, C.E. *et al.* Critical Review of Health Impacts of Wildfire Smoke Exposure. *Environ Health Perspect* **124**, 1334-1343 (2016).
2. Rappold, A.G. *et al.* Cardio-respiratory outcomes associated with exposure to wildfire smoke are modified by measures of community health. *Environ Health* **11**, 71 (2012).
3. Reid, C.E. *et al.* Differential respiratory health effects from the 2008 northern California wildfires: A spatiotemporal approach. *Environ Res* **150**, 227-235 (2016).

4. Tinling, M.A., West, J.J., Cascio, W.E., Kilaru, V. & Rappold, A.G. Repeating cardiopulmonary health effects in rural North Carolina population during a second large peat wildfire. *Environ Health* **15**, 12 (2016).

5. Wettstein, Z.S. *et al.* Cardiovascular and Cerebrovascular Emergency Department Visits Associated With Wildfire Smoke Exposure in California in 2015. *J Am Heart Assoc* **7** (2018).

6. Davies, I.P., Haugo, R.D., Robertson, J.C. & Levin, P.S. The unequal vulnerability of communities of color to wildfire. *PLoS One* **13**, e0205825 (2018).

7. Iaccarino, L. *et al.* Association Between Ambient Air Pollution and Amyloid Positron Emission Tomography Positivity in Older Adults With Cognitive Impairment. *JAMA Neurol* **78**, 197-207 (2021).

8. Cacciottolo, M. *et al.* Particulate air pollutants, APOE alleles and their contributions to cognitive impairment in older women and to amyloidogenesis in experimental models. *Transl Psychiatry* **7**, e1022 (2017).

9. Younan, D. *et al.* Particulate matter and episodic memory decline mediated by early neuroanatomic biomarkers of Alzheimer's disease. *Brain* **143**, 289-302 (2020).

10. Braithwaite, I., Zhang, S., Kirkbride, J.B., Osborn, D.P.J. & Hayes, J.F. Air Pollution (Particulate Matter) Exposure and Associations with Depression, Anxiety, Bipolar, Psychosis and Suicide Risk: A Systematic Review and Meta-Analysis. *Environ Health Perspect* **127**, 126002 (2019).

11. Lautrup, S., Sinclair, D.A., Mattson, M.P. & Fang, E.F. NAD(+) in Brain Aging and Neurodegenerative Disorders. *Cell Metab* **30**, 630-655 (2019).

12. Oh, S.J. *et al.* Evaluation of the neuroprotective effect of taurine in Alzheimer's disease using functional molecular imaging. *Sci Rep* **10**, 15551 (2020).

13. Jakaria, M. *et al.* Taurine and its analogs in neurological disorders: Focus on therapeutic potential and molecular mechanisms. *Redox Biol* **24**, 101223 (2019).

14. Aragon, M.J. *et al.* Serum-borne bioactivity caused by pulmonary multiwalled carbon nanotubes induces neuroinflammation via blood-brain barrier impairment. *Proc Natl Acad Sci U S A* **114**, E1968-E1976 (2017).

15. Mostovenko, E. *et al.* Carbon Nanotube Exposure Triggers a Cerebral Peptidomic Response: Barrier Compromise, Neuroinflammation and a Hyperexcited State. *Toxicol Sci* (2021).

16. Mostovenko, E. *et al.* Nanoparticle exposure driven circulating bioactive peptidome causes systemic inflammation and vascular dysfunction. *Part Fibre Toxicol* **16**, 20 (2019).

17. Engelhardt, B., Vajkoczy, P. & Weller, R.O. The movers and shapers in immune privilege of the CNS. *Nat Immunol* **18**, 123-131 (2017).

18. Yousef, H. *et al.* Aged blood impairs hippocampal neural precursor activity and activates microglia via brain endothelial cell VCAM1. *Nat Med* **25**, 988-1000 (2019).

19. Sun, L. *et al.* Ambient fine particulate matter and ozone exposures induce inflammation in epicardial and perirenal adipose tissues in rats fed a high fructose diet. *Part Fibre Toxicol* **10**, 43 (2013).

20. Agency, U.S.E.P. Reference method for the determination of fine particulate matter as PM2.5 in the atmosphere. *Washington, DC: EPA 40 CFR Part 50, Appendix L.*; 1997.

21. Harkema, J.R. *et al.* Effects of concentrated ambient particles and diesel engine exhaust on allergic airway disease in Brown Norway rats. *Res Rep Health Eff Inst*, 5-55 (2009).

22. Simpson, C.D., Dills, R.L., Katz, B.S. & Kalman, D.A. Determination of levoglucosan in atmospheric fine particulate matter. *J Air Waste Manage* **54**, 689-694 (2004).

23. Tyler, C.R. *et al.* Aging Exacerbates Neuroinflammatory Outcomes Induced by Acute Ozone Exposure. *Toxicol Sci* **163**, 123-139 (2018).

24. Carroll, P.A. *et al.* Deregulated Myc Requires MondoA/Mlx for Metabolic Reprogramming and Tumorigenesis. *Cancer Cell* **27**, 271-285 (2015).

25. Gu, H., Zhang, P. & Raftery, D. Globally Optimized Targeted Mass Spectrometry (GOT-MS): Reliable Metabolomics Analysis with Broad Coverage *Anal. Chem.* **87**, 12355–12362 (2015).

26. Gu, H. *et al.* Quantitative Method to Investigate the Balance between Metabolism and Proteome Biomass: Starting from Glycine. *Angew. Chem. Int. Ed. Engl.* **55**, 15646-15650 (2016).

27. Shi, X.J. *et al.* Database-Assisted Globally Optimized Targeted Mass Spectrometry (dGOT-MS): Broad and Reliable Metabolomics Analysis with Enhanced Identification. *Anal. Chem.* **91**, 13737-13745 (2019).

28. Jasbi, P. *et al.* Coccidioidomycosis Detection Using Targeted Plasma and Urine Metabolic Profiling. *J. Proteome Res.* **18**, 2791-2802 (2019).

29. Eghlimi, R., Shi, X.J., Hrovat, J., Xi, B.W. & Gu, H.W. Triple Negative Breast Cancer Detection Using LC-MS/MS Lipidomic Profiling. *J. Proteome Res.* **19**, 2367-2378 (2020).

30. Verma, V. *et al.* Physicochemical and toxicological profiles of particulate matter in Los Angeles during the October 2007 southern California wildfires. *Environ Sci Technol* **43**, 954-960 (2009).

31. Ahmadi, Z., Arababadi, M.K. & Hassanshahi, G. CXCL10 activities, biological structure, and source along with its significant role played in pathophysiology of type I diabetes mellitus. *Inflammation* **36**, 364-371 (2013).

32. McReynolds, M.R., Chellappa, K. & Baur, J.A. Age-related NAD(+) decline. *Exp Gerontol* **134**, 110888 (2020).

33. Genovese, I. *et al.* Sorcin is an early marker of neurodegeneration, Ca(2+) dysregulation and endoplasmic reticulum stress associated to neurodegenerative diseases. *Cell Death Dis* **11**, 861 (2020).

34. Wimmer, I. *et al.* PECAM-1 Stabilizes Blood-Brain Barrier Integrity and Favors Paracellular T-Cell Diapedesis Across the Blood-Brain Barrier During Neuroinflammation. *Front Immunol* **10**, 711 (2019).

35. Schuller, A. & Montrose, L. Influence of Woodsmoke Exposure on Molecular Mechanisms Underlying Alzheimer's Disease: Existing Literature and Gaps in Our Understanding. *Epigenet Insights* **13**, 2516865720954873 (2020).

36. Farugia, T.L., Cuni-Lopez, C. & White, A.R. Potential Impacts of Extreme Heat and Bushfires on Dementia. *J Alzheimers Dis* **79**, 969-978 (2021).

37. Liu, Y. *et al.* Health Impact Assessment of PM 2.5 attributable mortality from the September 2020 Washington State Wildfire Smoke Episode. *medRxiv* (2020).

38. Liu, Y. *et al.* Health Impact Assessment of the 2020 Washington State Wildfire Smoke Episode: Excess Health Burden Attributable to Increased PM2.5 Exposures and Potential Exposure Reductions. *Geohealth* **5**, e2020GH000359 (2021).

39. Chang, K.H. *et al.* Increased risk of dementia in patients exposed to nitrogen dioxide and carbon monoxide: a population-based retrospective cohort study. *PLoS One* **9**, e103078 (2014).

40. Aragon, M. *et al.* MMP-9-Dependent Serum-Borne Bioactivity Caused by Multiwalled Carbon Nanotube Exposure Induces Vascular Dysfunction via the CD36 Scavenger Receptor. *Toxicol Sci* **150**, 488-498 (2016).

41. Robertson, S. *et al.* CD36 mediates endothelial dysfunction downstream of circulating factors induced by O3 exposure. *Toxicol Sci* **134**, 304-311 (2013).

42. Aragon, M.J. *et al.* Inflammatory and Vasoactive Effects of Serum Following Inhalation of Varied Complex Mixtures. *Cardiovasc Toxicol* **16**, 163-171 (2016).

43. Winneberger, J. *et al.* Platelet endothelial cell adhesion molecule-1 is a gatekeeper of neutrophil transendothelial migration in ischemic stroke. *Brain Behav Immun* **93**, 277-287 (2021).

44. Schetters, S.T.T., Gomez-Nicola, D., Garcia-Vallejo, J.J. & Van Kooyk, Y. Neuroinflammation: Microglia and T Cells Get Ready to Tango. *Front Immunol* **8**, 1905 (2017).

45. Wyss-Coray, T. & Mucke, L. Inflammation in neurodegenerative disease--a double-edged sword. *Neuron* **35**, 419-432 (2002).

46. Schwartz, M. & Baruch, K. The resolution of neuroinflammation in neurodegeneration: leukocyte recruitment via the choroid plexus. *EMBO J* **33**, 7-22 (2014).

47. Oudin, A., Segersson, D., Adolfsson, R. & Forsberg, B. Association between air pollution from residential wood burning and dementia incidence in a longitudinal study in Northern Sweden. *PLoS One* **13**, e0198283 (2018).

48. Greaves, C.V. & Rohrer, J.D. An update on genetic frontotemporal dementia. *J Neurol* **266**, 2075-2086 (2019).

49. Jansen, I.E. *et al.* Genome-wide meta-analysis identifies new loci and functional pathways influencing Alzheimer's disease risk. *Nat Genet* **51**, 404-413 (2019).

50. Gatz, M. *et al.* Role of genes and environments for explaining Alzheimer disease. *Arch Gen Psychiatry* **63**, 168-174 (2006).

51. Patten, K.T. *et al.* The Effects of Chronic Exposure to Ambient Traffic-Related Air Pollution on Alzheimer's Disease Phenotypes in Wildtype and Genetically Predisposed Male and Female Rats. *Environ Health Perspect* **129**, 57005 (2021).

52. Newman, A.B. & Murabito, J.M. The epidemiology of longevity and exceptional survival. *Epidemiol Rev* **35**, 181-197 (2013).

53. Shadyab, A.H. & LaCroix, A.Z. Genetic factors associated with longevity: a review of recent findings. *Ageing Res Rev* **19**, 1-7 (2015).

54. Zeng, Y. *et al.* Novel loci and pathways significantly associated with longevity. *Sci Rep* **6**, 21243 (2016).

55. Wyss-Coray, T. Ageing, neurodegeneration and brain rejuvenation. *Nature* **539**, 180-186 (2016).

56. Ivanisevic, J. *et al.* Metabolic drift in the aging brain. *Aging (Albany NY)* **8**, 1000-1020 (2016).

57. Fang, E.F. *et al.* NAD(+) Replenishment Improves Lifespan and Healthspan in Ataxia Telangiectasia Models via Mitophagy and DNA Repair. *Cell Metab* **24**, 566-581 (2016).

58. Hou, Y. *et al.* NAD(+) supplementation normalizes key Alzheimer's features and DNA damage responses in a new AD mouse model with introduced DNA repair deficiency. *Proc Natl Acad Sci U S A* **115**, E1876-E1885 (2018).

59. Kane, A.E. & Sinclair, D.A. Sirtuins and NAD(+) in the Development and Treatment of Metabolic and Cardiovascular Diseases. *Circ Res* **123**, 868-885 (2018).

60. Bhat, M.A. *et al.* Expedition into Taurine Biology: Structural Insights and Therapeutic Perspective of Taurine in Neurodegenerative Diseases. *Biomolecules* **10** (2020).

61. Verdin, E. NAD(+) in aging, metabolism, and neurodegeneration. *Science* **350**, 1208-1213 (2015).

62. Giorgi-Coll, S., Amaral, A.I., Hutchinson, P.J.A., Kotter, M.R. & Carpenter, K.L.H. Succinate supplementation improves metabolic performance of mixed glial cell cultures with mitochondrial dysfunction. *Sci Rep* **7**, 1003 (2017).

63. El Idrissi, A., Shen, C.H. & L'Amoreaux W, J. Neuroprotective role of taurine during aging. *Amino Acids* **45**, 735-750 (2013).

64. Ruminski, M. & Kondragunta, S. Monitoring fire and smoke emissions with the hazard mapping system. *Proc Spie* **6412** (2006).

65. Ruminski, M.K., S.; Draxler, R.; Zeng, J. Recent changes to the Hazard Mapping System. *15th International Emission Inventory Conference: Reinventing Inventories—New Ideas in New Orleans*. New Orleans, LA: EPA; 2006.

66. Ruminski, M.K., S.; Draxler, R.; Rolph, G. . Use of environmental satellite imagery for smoke depiction and transport model initialization. *16th Annual International Emission Inventory Conf.: Emission Inventories—Integration, Analysis, and Communications*. Raleigh, NC: EPA; 2007.

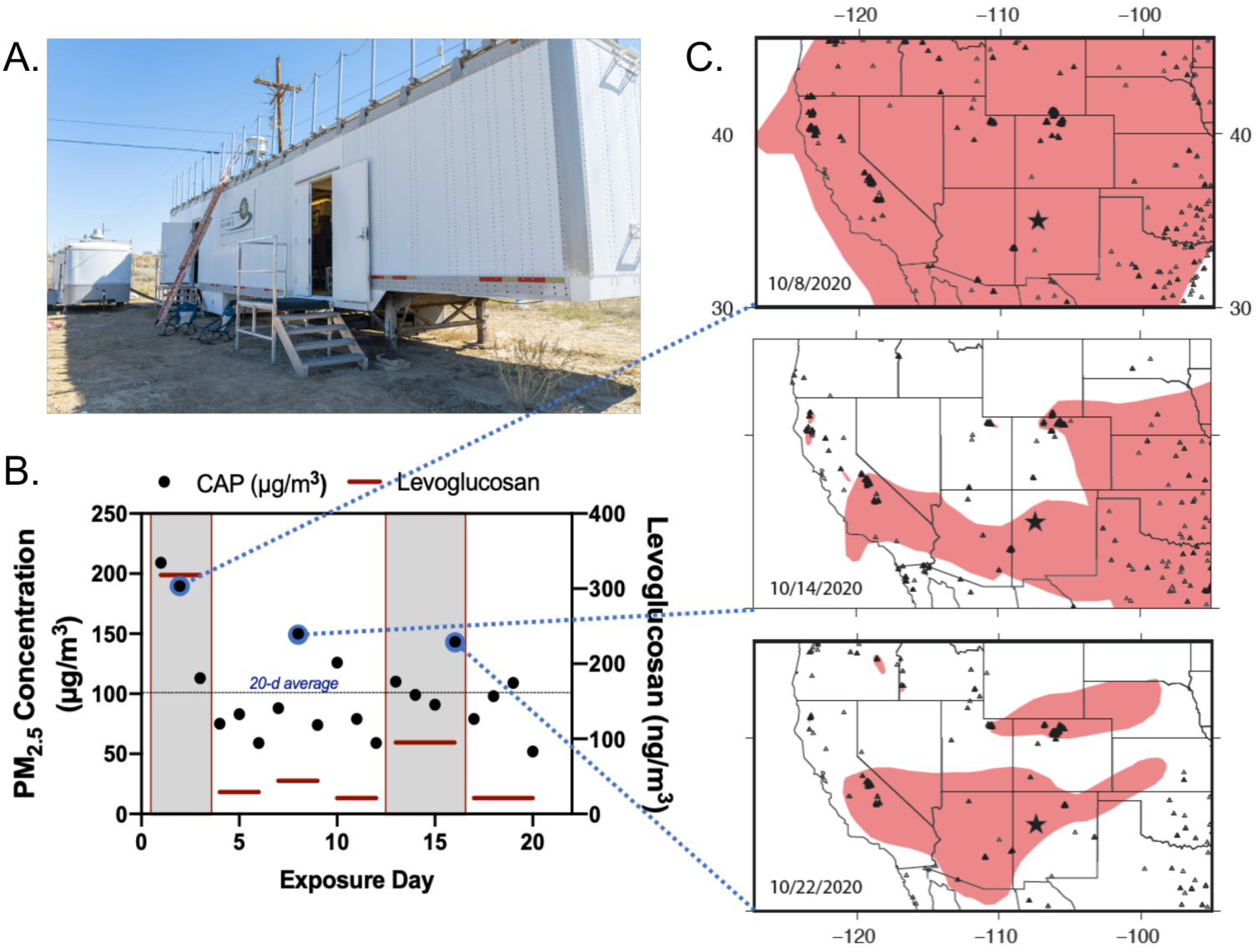

Figure 1. Exposure to concentrated particulates in Paguate, NM. A. Mobile laboratory containing rodent exposure chambers and a Harvard-type particle concentrator. B. Daily PM2.5 gravimetric mass concentrations for the 20 days of exposure (black dots), along with levoglucosan measures (red bars) that span 3-4 days, as filters were pooled to provide sufficient material. C. Smoke and wildfire locations for 3 representative days in October 2020 derived from the National Oceanic and Atmospheric Administration Hazard Mapping System (HMS) Fire and Smoke Product [58, 59, 60], with dashed lines indicating the link to exposures days in B. The black star indicates the location of Paguate, NM. Smoke plumes shown in pink were derived manually from geostationary and polar-orbiting satellites and represent a minimum smoke PM2.5 concentration of 5 µg/m3. Fire locations shown by triangles were obtained with automated fire detection algorithms [59].

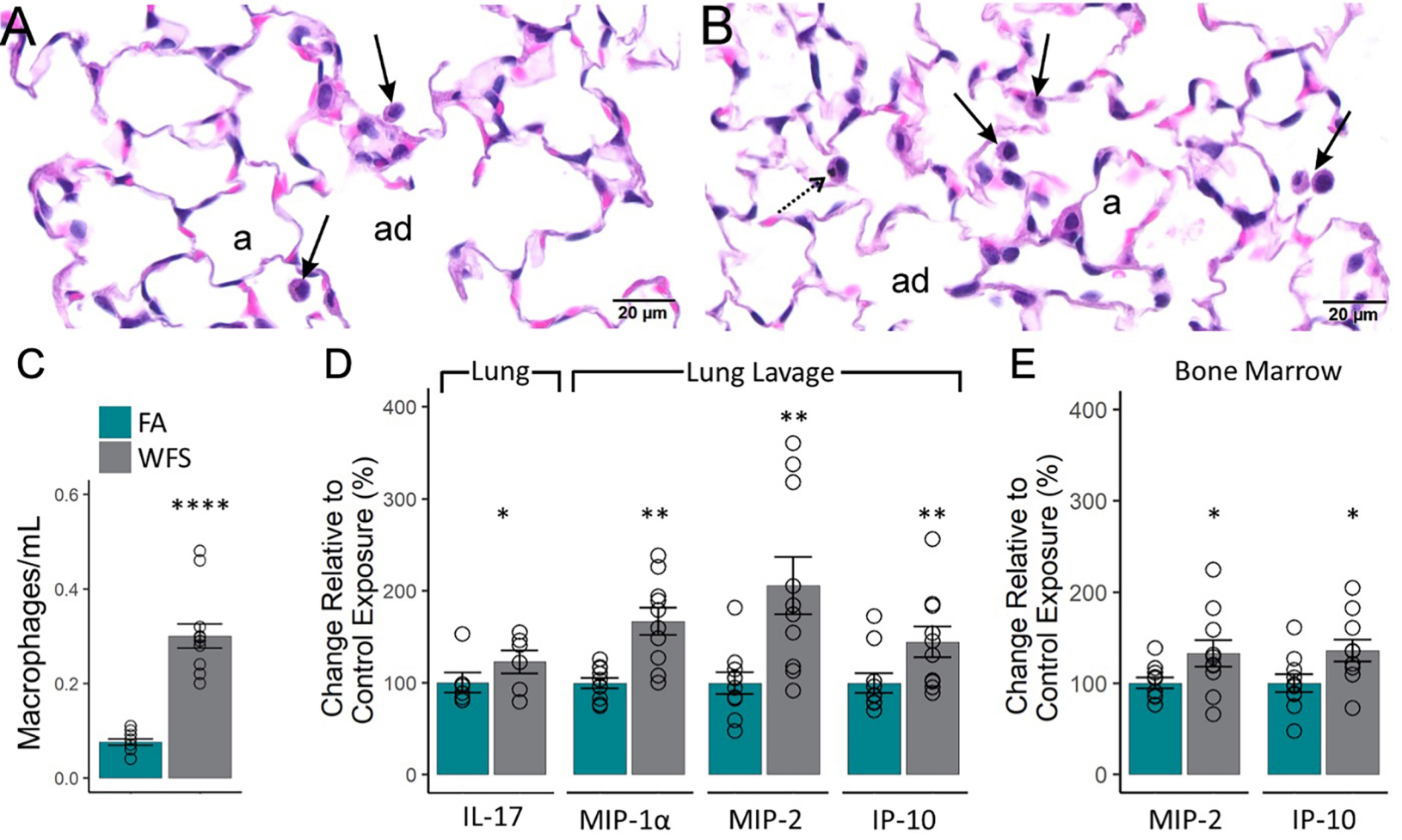

Figure 2. Significant pulmonary and bone marrow cytokine responses to 20-day exposure to wildfire smoke (WFS). Light photomicrographs of hematoxylin and eosin-stained lung tissue from the left lung lobe of mice exposed to **A)** filtered air or **B)** concentrated fine ambient particles. Slightly more alveolar macrophages (arrows) were present in WFS-exposed mice than filtered air control mice. Stippled arrow, particle laden-alveolar macrophage (black cytoplasmic material); Sold arrow, alveolar macrophage without cytoplasmic particles; a, alveolus; ad, alveolar duct. **C.** Airway macrophages in bronchoalveolar lavage fluid were significantly elevated after WFS exposure. **D.** Whole lung cytokine IL-17, and Bronchoalveolar lavage cytokines, MIP-1a, MIP-2, and IP-10 were significantly elevated by WFS. **E.** Bone marrow concentrations of MIP-2 and IP-10 were elevated by WFS. All measured cytokines are provided in Supplemental Tables 2-5.

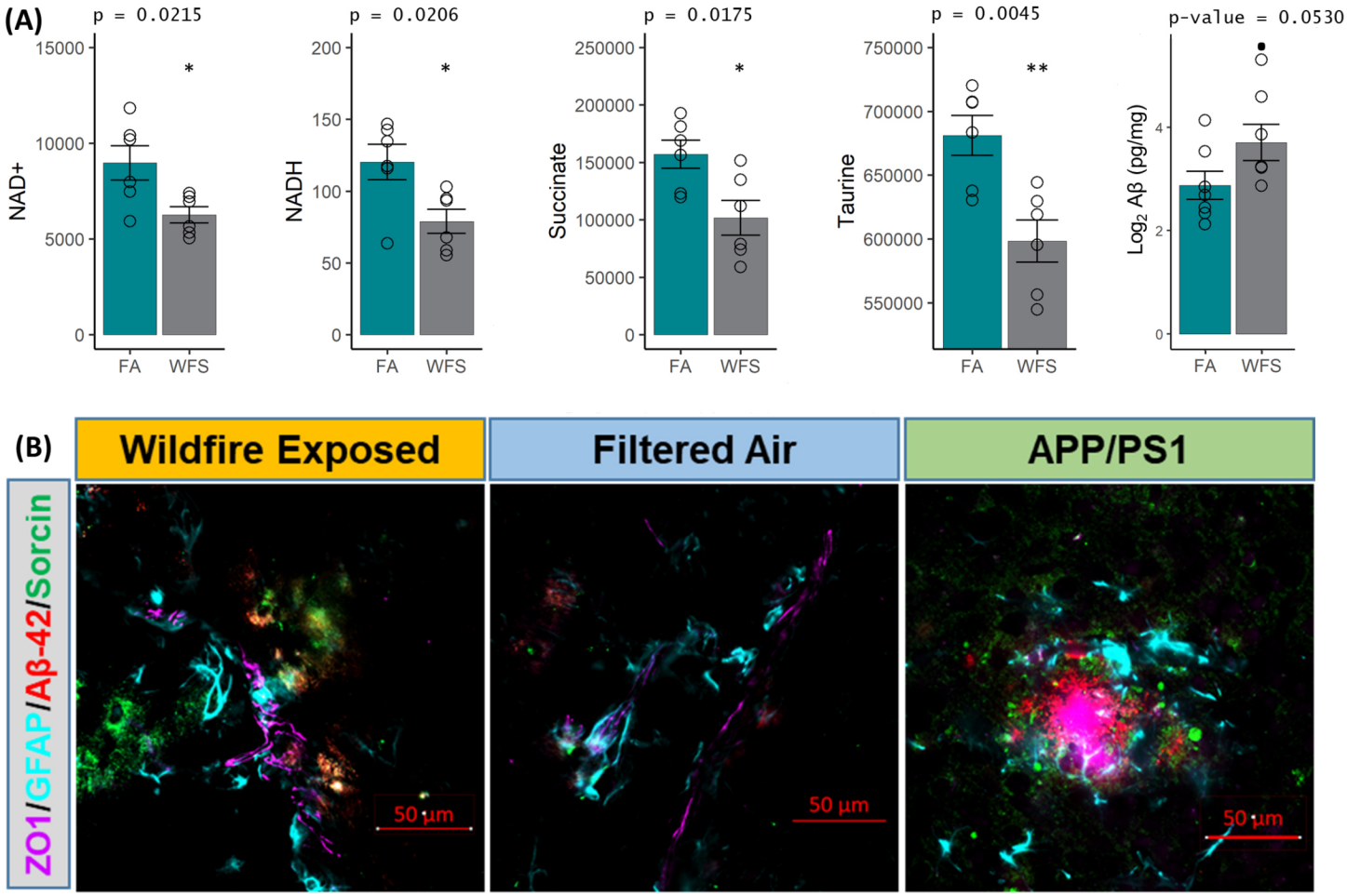

Figure 3. Markers related to aging and neurodegeneration/disease. **(A)** NAD^+, NADH, Succinate, and Taurine were all downregulated and amyloid beta (Aβ) levels were upregulated in WFS-exposed mice. NAD^+ is involved in stress resistance, synaptic plasticity and is downregulated in aged animals, while the conversion of NAD^+ to NADH is important for ATP generation[11]. Succinate is important for mitochondrial function and oxidative metabolism[61]. Taurine has been shown to be neuroprotective during aging[62]**.** Aβ in humans is a precursor to Alzheimer's. The existence of murine Aβ can occur with injury, as mice do not naturally form plaques. **(B)** Representative image of neurodegenerative pathogenic markers found at the neocortical neurovascular units in WFS-exposed mice. Brain Aβ-42 (red) increases in WFS-exposed C57 mice proximal to the neurovascular unit (ZO1). Additionally, the early pathogenic marker Sorcin increased (green), indicating ER stress / unfolded protein responses.

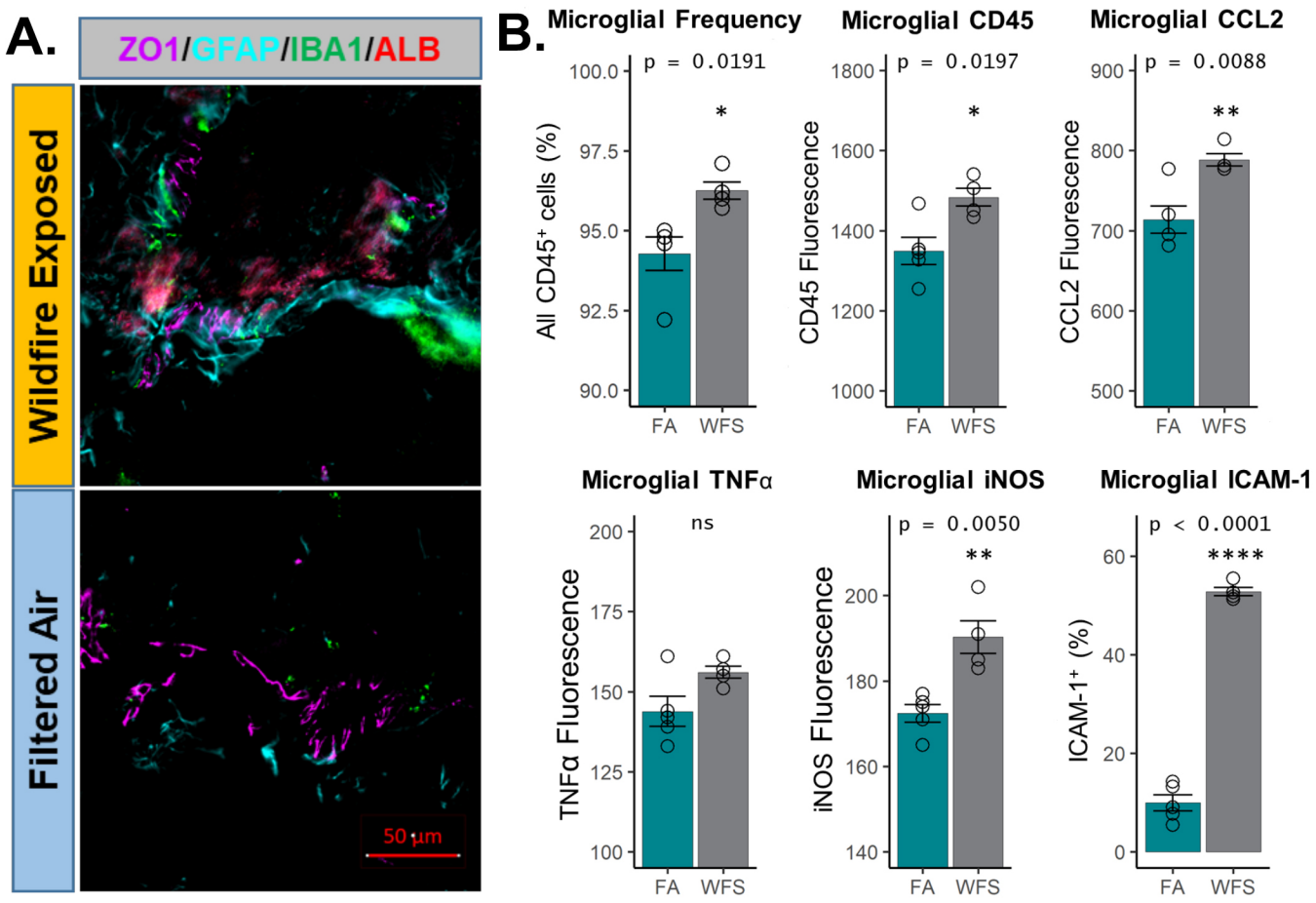

Figure 4: A. Immunohistochemical staining revealing reactive astrogliosis (Glial Fibrillary Acidic Protein; GFAP; cyan) and microglial activation/invasion (ionized calcium binding adaptor molecule 1; Iba1; green) along the neurovascular unit (zonula occludens 1; ZO1 purple) in WFS-exposed brains, with negligible staining of GFAP or Iba1 in filtered air control mice. Albumin (red) demarcates BBB impairment and protein leakage into the parenchyma. **B.** Percentage of microglia and their surface expression levels of CD45, adhesion molecule ICAM-1 and intracellular levels of proinflammatory factors, iNOS, TNF-α and CCL2 were analyzed. N=4-5 mice per group. Mean and standard error are shown.

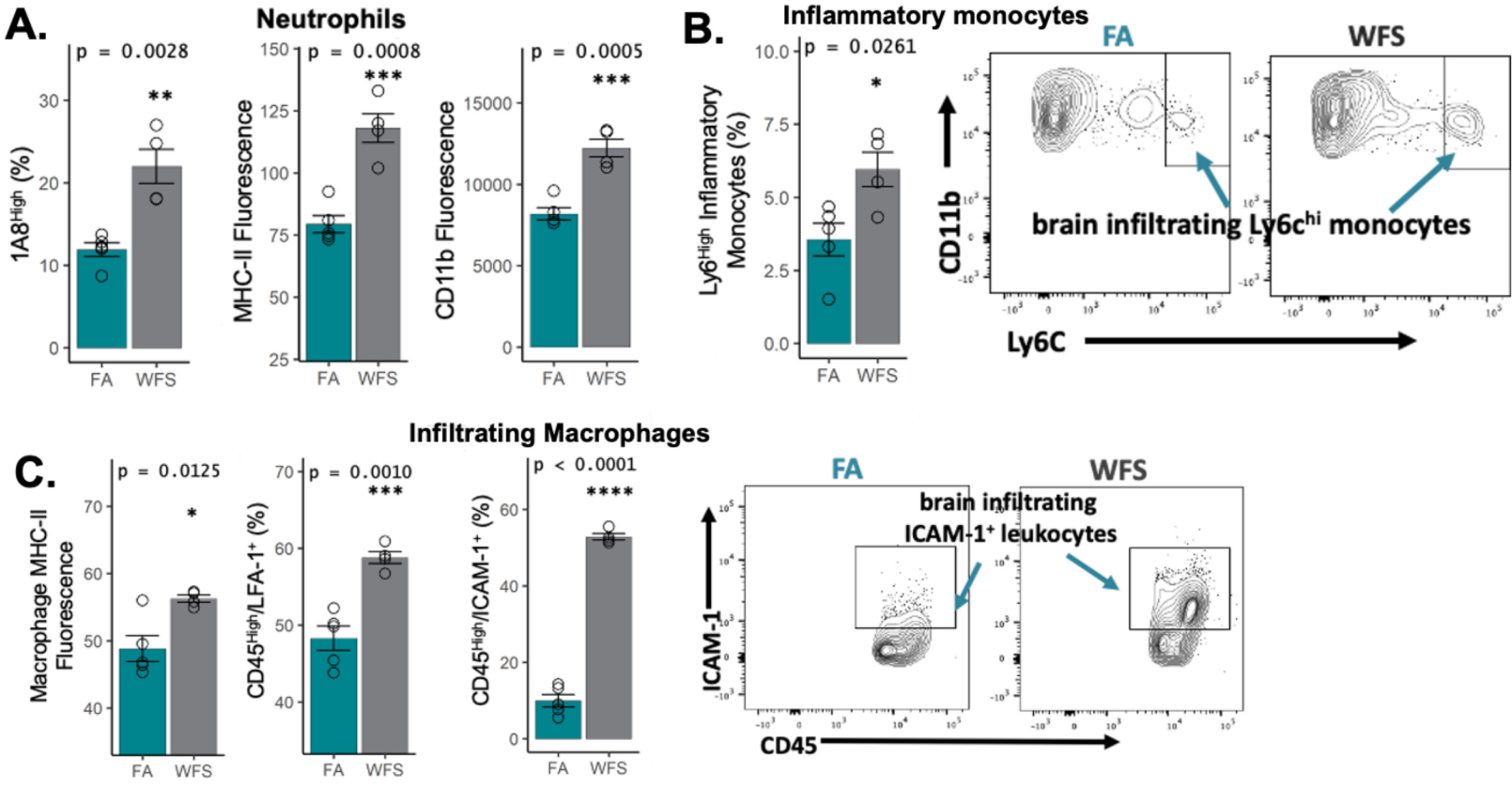

Figure 5: A. Increased frequency of mature neutrophils (with high expression of 1A8), along with overall increase in MHC2 and CD11b surface expression of all $CD45^{+}1A8^{+}$ neutrophils in the brain due to WFS exposure. **B.** Inflammatory monocytes in the brain were increased in frequency with WFS exposure. **C.** CNS infiltrating $CD45^{high}CD11b^{+}$ macrophage/monocyte population shows increased MHC2 expression and frequency of LFA-1+ and ICAM-1+ peripheral leukocytes were also increased due to WFS exposure, N=4-5 mice per group. Mean and standard error are shown.

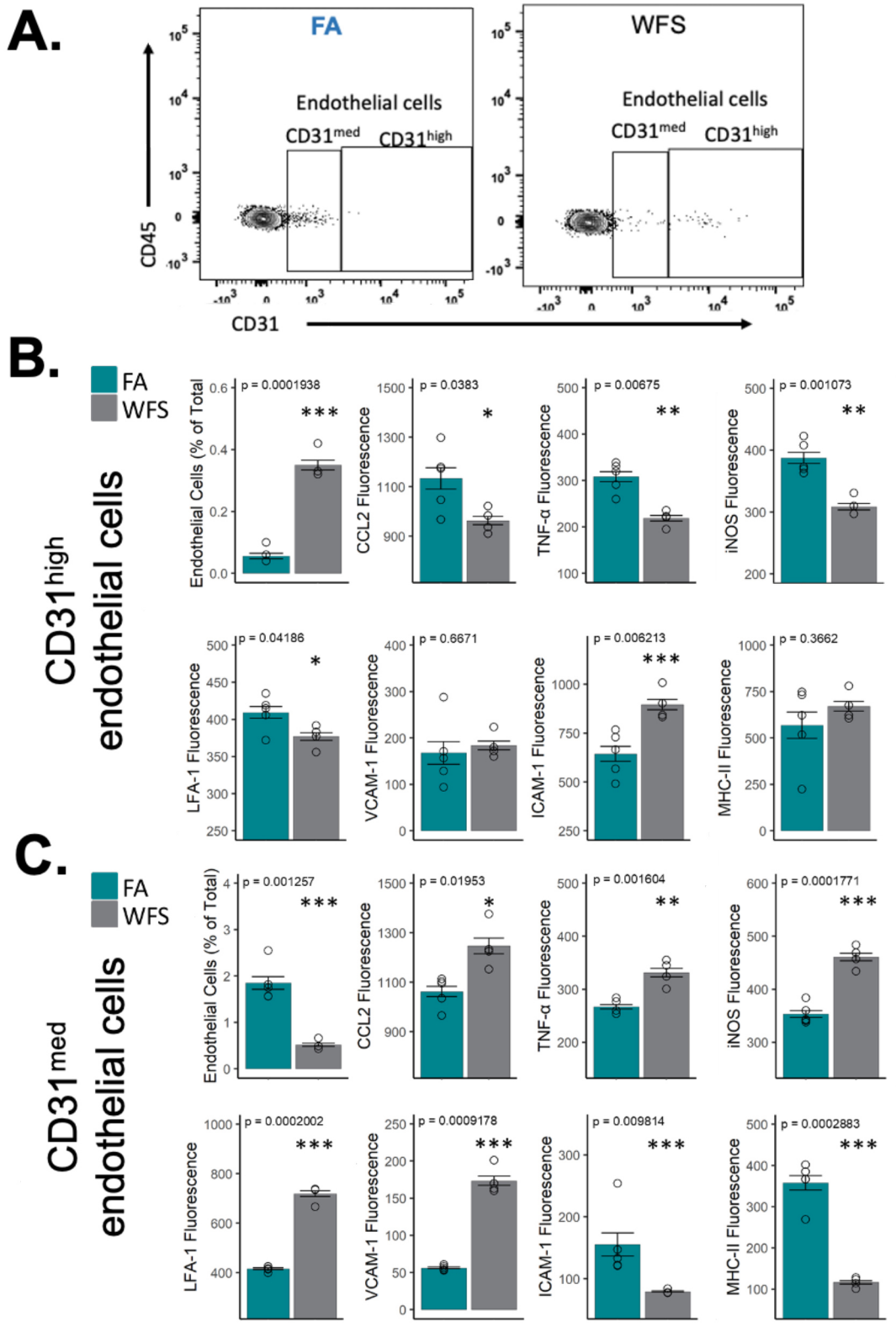

Figure 6: Cerebrovascular endothelial cells exhibit a herterogeneous inflammatory response to WFS. A. Representative flow cytometry plots of endothelial cells (with medium and high expression of CD31/PECAM-1 on $CD45^-$ cells) in the brain in FA or WFS exposure group. These two subsets of endothelial cells displayed comparatively different neuroimmune activity profile, as detailed in B-C. **B.** Frequency of endothelial cells with high expression of CD31 was increased following WFS exposure, however, these endothelial cells displayed reduced levels of these proinflammatory factors. Increased frequency of ICAM-1 expressing endothelial cells were observed due to WFS exposure in this endothelial subset despite no changes in MHC2. N=4-5 mice per group. Mean and standard error are shown. **C.** Frequency of $CD31^{med}$ endothelial were reduced following WFS exposure, however, these cells displayed increased proinflammatory phenotype such as increased levels of CCL2, TNF and iNOS, although reduced levels of ICAM-1 and MHC2 were observed.

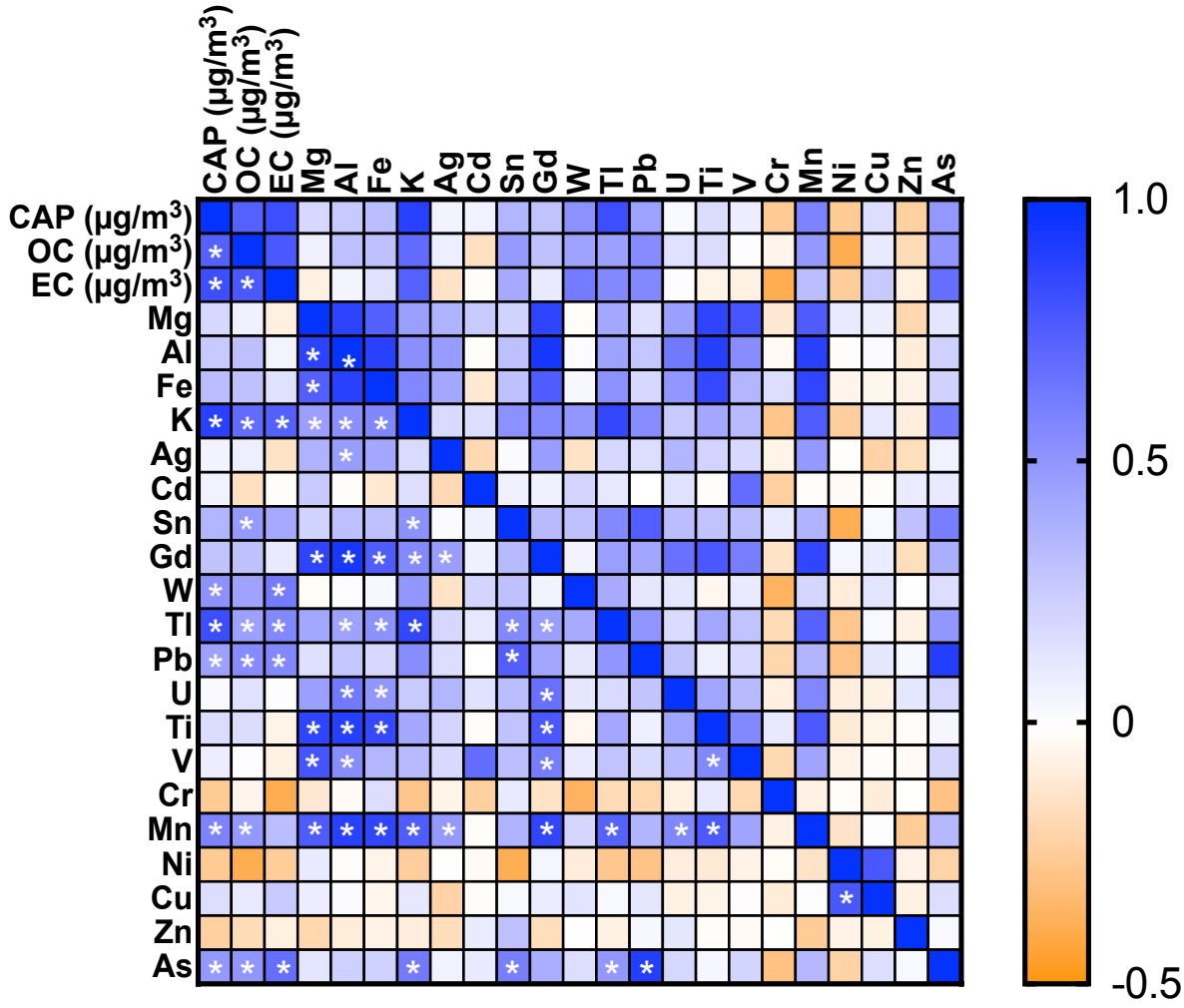

Supplemental Figure 1. Pearson's correlation analysis of elemental composition of PM2.5 across the 20 days of exposure. Asterisks indicate significant association ($p<0.05$). Clusters of elements that line up with previous reports of wildfire composition, including potassium, magnesium, and manganese were noted, while days with lower wildfire smoke contribution exhibited clustering of crustal elements (iron, aluminum, rare earth metals) common to the rural southwestern United States.

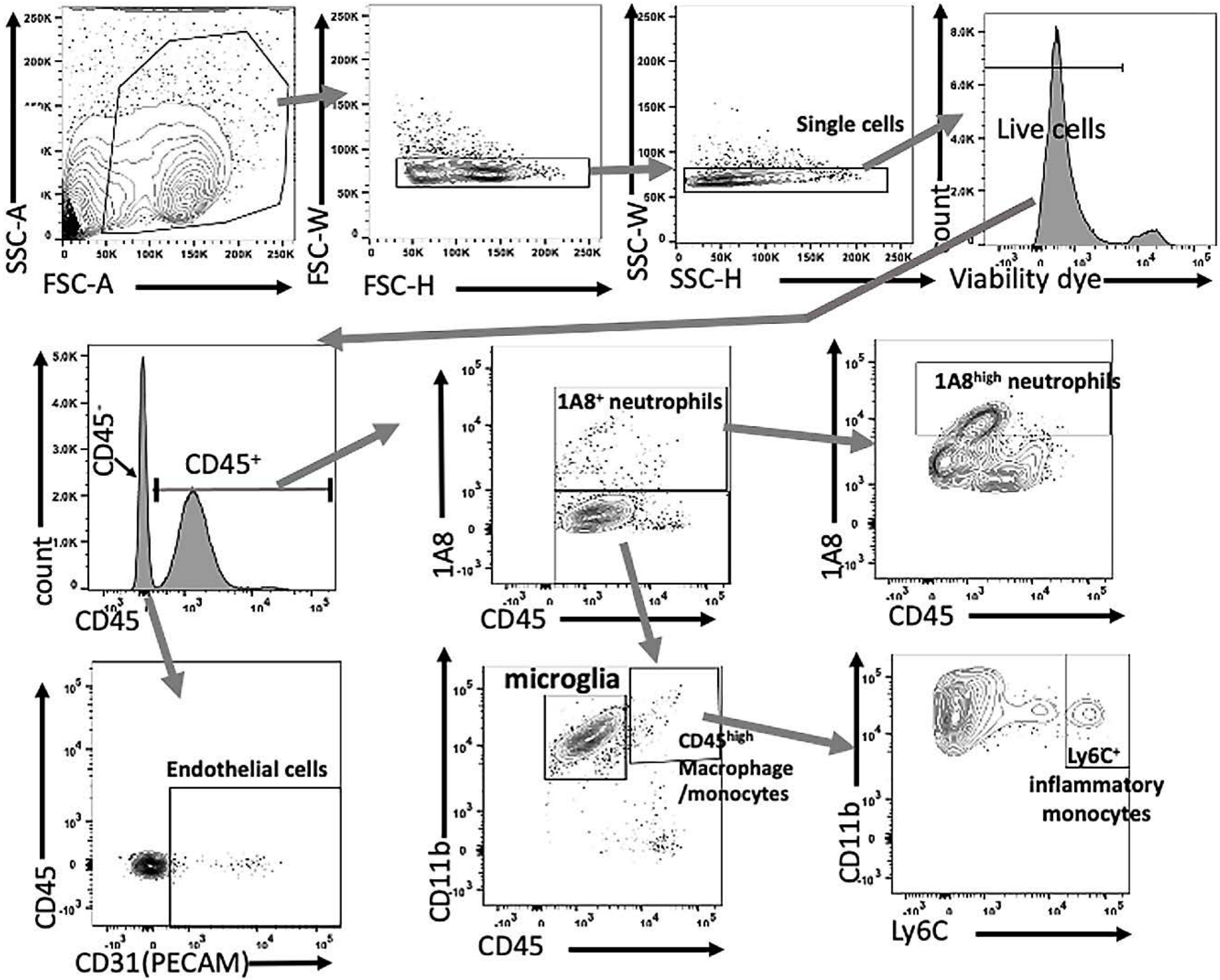
SSC-A
FSC-A
FSC-W
FSC-H
SSC-W
SSC-H
Single cells
Live cells
count
Viability dye
CD45-
CD45+
count
CD45
1A8+ neutrophils
1A8
CD45
1A8high neutrophils
1A8
CD45
Endothelial cells
CD45
CD31(PECAM)
microglia
CD45high
Macrophage
/monocytes
CD11b
CD45
Ly6C+
inflammatory
monocytes
CD11b
Ly6C

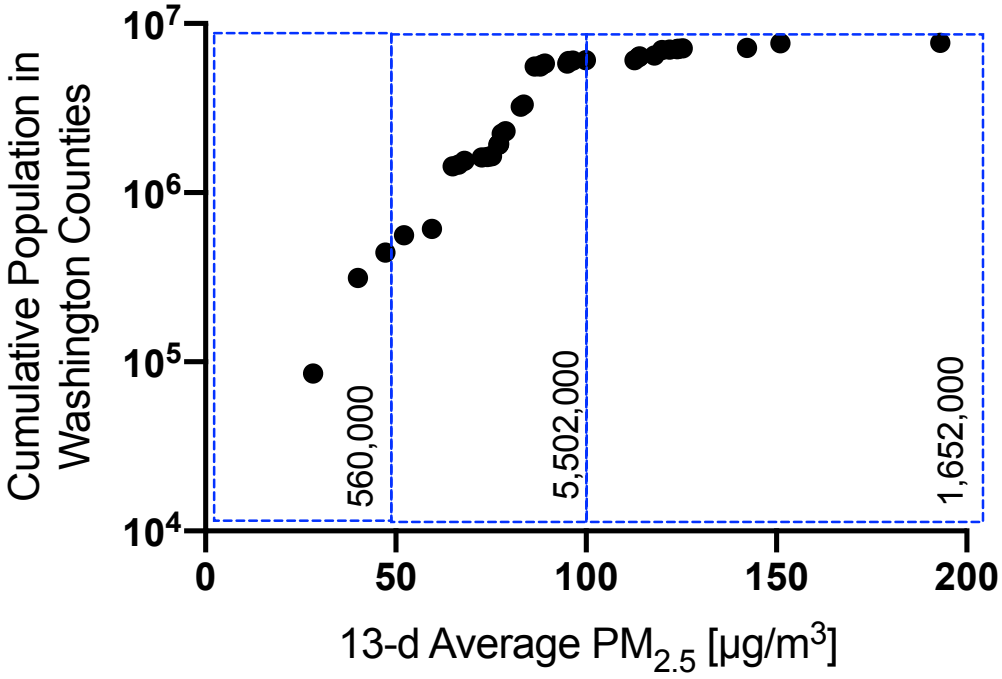

Figure S3. Reanalysis of data reported by Liu and colleagues[35,36] from September 2020 wildfires revealed over 1.6 million people in Washington state were exposed to concentrations in excess of 100 µg/m^3 for the 13-day period.

Supplemental Table 1: PM2.5 Metal Composition

Date	CAP (μg/m³)	OC (μg/m³)	EC (μg/m³)	Levoglucosan (ng/m³)	(μg/m³)				(ng/m³)														
					Mg	Al	Fe	K	Ag	Cd	Sn	Gd	W	Tl	Pb	U	Ti	V	Cr	Mn	Ni	Cu	Zn	As
10/7/20	209	127	2.08	318	0.47	0.72	0.90	1.99	0.06	0.79	0.61	0.14	2.06	0.06	6.30	0.07	17.23	1.22	66.4	48.7	3.28	23.26	85.4	2.4
10/8/20	191	120	2.1		0.47	0.70	0.87	1.67	0.04	0.81	0.39	0.12	0.45	0.05	7.06	0.06	18.30	1.34	60.1	44.1	3.03	34.05	76.5	3.5
10/9/20	113	84	1.02		0.57	0.84	0.81	1.37	0.06	1.08	0.86	0.20	0.17	0.04	13.54	0.09	17.96	1.95	73.0	40.2	3.77	24.53	107.0	5.3
10/10/20	75	93	BD	29	0.33	0.52	0.44	0.81	0.07	0.44	0.27	0.09	0.06	BD	4.27	0.05	13.55	1.08	125.3	28.6	4.97	22.63	79.2	1.4
10/11/20	83	77	0.14		0.52	0.66	0.60	0.83	0.06	0.57	0.57	0.14	0.42	0.01	5.73	0.12	18.09	1.63	121.4	34.6	2.89	23.12	75.1	1.3
10/12/20	59	46	BD		0.70	0.83	1.07	0.88	0.10	0.42	0.24	0.12	0.16	0.01	2.85	0.06	26.95	1.89	94.0	36.2	6.30	16.62	79.8	1.1
10/13/20	88	67	BD	44	0.25	0.31	0.26	0.36	0.08	0.19	BD	0.04	BD	BD	4.30	0.03	7.64	0.51	96.1	12.7	2.39	13.62	88.4	0.3
10/14/20	149	41	BD		0.56	0.67	0.78	1.29	0.04	1.37	0.16	0.12	0.19	0.06	3.54	0.07	20.86	1.29	100.7	46.3	4.93	17.05	49.1	1.1
10/15/20	74	52	BD		0.53	0.66	0.81	0.77	0.09	0.45	0.23	0.13	0.23	0.03	3.52	0.07	19.20	1.29	85.2	38.3	5.92	14.68	35.9	1.0
10/16/20	126	86	BD	21	0.86	1.32	1.33	1.48	0.50	0.30	0.42	0.26	0.17	0.05	7.06	0.12	28.95	2.37	92.9	68.2	6.47	14.63	58.4	2.1
10/17/20	79	45	BD		0.58	0.67	0.66	0.74	0.06	0.44	BD	0.14	0.37	0.01	3.28	0.06	15.41	1.18	91.6	30.0	31.93	60.83	51.2	1.0
10/18/20	59	54	BD		0.44	0.77	0.87	0.81	0.05	1.66	0.10	0.13	0.24	BD	2.95	0.12	17.89	1.15	91.0	31.8	9.26	18.50	305.3	1.2
10/19/20	110	85	BD	95	0.69	1.00	0.95	1.34	0.06	0.75	0.51	0.16	0.22	0.03	4.81	0.08	27.01	1.56	105.3	42.1	5.98	21.38	111.6	1.2
10/20/20	99	75	BD		0.53	0.85	1.02	0.88	0.05	0.32	0.48	0.14	0.06	0.02	3.88	0.07	23.80	1.31	226.4	40.5	8.27	23.78	68.8	1.1
10/21/20	91	87	BD		0.60	0.91	1.17	0.99	0.05	0.35	0.32	0.16	0.28	0.03	4.16	0.08	29.12	1.48	190.5	45.0	3.00	16.87	57.6	1.3
10/22/20	143	110	0.92		0.84	1.31	1.18	1.41	0.06	0.54	0.67	0.24	0.84	0.05	7.54	0.12	36.90	2.27	67.3	64.9	4.81	32.11	85.4	1.8
10/23/20	79	52	BD	21	0.49	0.66	0.73	0.95	0.04	0.43	0.83	0.11	0.47	0.04	5.47	0.06	23.94	1.79	112.8	29.5	4.81	22.71	359.3	1.6
10/24/20	98	59	BD		0.76	0.74	0.65	1.10	0.05	4.36	0.46	0.15	0.83	0.03	4.38	0.08	20.63	4.03	81.2	35.2	6.34	22.77	86.6	1.5
10/25/20	109	68	BD		0.87	1.09	0.96	1.21	0.05	0.99	BD	0.23	0.13	0.02	3.02	0.07	33.13	2.76	62.7	48.1	7.56	19.51	59.3	1.4
10/26/20	52	48	BD		0.32	0.58	0.49	0.48	0.06	0.37	BD	0.10	0.80	BD	2.19	0.08	13.20	0.89	58.3	24.0	6.12	14.64	56.3	0.9

Supplemental Table 2. Cytokine analysis from Bronchoalveolar Lavage Fluid

Bronchoalveolar Lavage Fluid (BALF)						
Parameter	**Units**	**FA Control Average**	**StDev**	**WFS Average**	**StDev**	**p-value**
IL-1b	pg/uL	0.4519325	0.059261382	0.52081375	0.152022257	0.3965
IL-4	pg/uL	0.320305182	0.151474264	0.304952091	0.101664765	0.79286
IL-5	pg/uL	1.01267175	0.223756557	1.076087833	0.240507016	0.52861
IL-6	pg/uL	8.145796167	2.134468234	8.5226095	1.669125646	0.64916
KC/Gro	pg/uL	6.030723583	1.925796871	7.513566167	2.061423529	0.09523
IL-10	pg/uL	1.535870417	0.491964558	1.553471833	0.481478049	0.93318
IL-12/70p	pg/uL	9.808917714	2.418022859	9.0249265	2.797161089	0.60047
TNFa	pg/uL	1.62360075	0.537530798	2.016501667	0.627158023	0.12892
IL-9	pg/uL	7.555480586	1.286814844	6.936610249	1.100932958	0.28739
MCP-1	pg/uL	1.360452398	0.312228314	1.547204956	0.347068925	0.24566
IL-33	pg/uL	3.635960251	1.416507684	4.088229137	1.002628311	0.44448
IL-27/p28/IL-30	pg/uL	2.843658648	0.64134539	2.922679686	0.578881159	0.78691
IL-15	pg/uL	45.69871521	10.94731435	50.87369654	9.031577515	0.28841
IL-17A/F	pg/uL	1.401698364	0.324463188	1.366126285	0.081035544	0.75332
MIP-1a	pg/uL	1.791371111	0.304258732	3.0085989	0.806490555	0.0005
MIP-2	pg/uL	1.530394834	0.54397422	3.166257725	1.443000978	0.00516
IP-10	pg/uL	2.199727	0.713061779	3.191308232	1.113195654	0.03718

Supplemental Table 3. Cytokine Analysis for Whole Lung

Lung						
Parameter	**Units**	**FA Control Average**	**StDev**	**WFS Average**	**StDev**	**p-value**
IL-9	pg/uL	23.48540725	7.006247659	23.31229685	4.859410321	0.96468
MCP-1	pg/uL	24.73462844	10.4202126	24.01974649	9.432535224	0.9117
IL-33	pg/uL	611.8416405	135.6606742	710.9677971	79.78146193	0.18934
IL-27/p28/IL-30	pg/uL	15.37996175	5.632020039	11.86273012	2.006138735	0.21771
IL-15	pg/uL	67.69983654	17.83893454	79.05666653	19.46422204	0.35881
IL-17A/F	pg/uL	4.655003398	1.139304469	5.701425293	1.312378815	0.20791
Mip-1a	pg/uL	34.44708036	10.49363603	29.91329971	9.182986455	0.48388
MIP-2	pg/uL	5.254933767	1.097111332	5.501019354	1.131487891	0.73422
IP-10	pg/uL	87.16771412	27.20893117	73.4398613	25.63038008	0.43067
IFNg	pg/uL	1.683506523	0.587375458	2.566530872	2.43739083	0.44923
IL-10	pg/uL	8.660157826	4.199058968	8.770448407	9.71841988	0.98187
IL-12p70	pg/uL	3.627856695	1.044689609	3.56493305	1.643018886	0.94382
IL-1b	pg/uL	1.555284304	0.958652685	1.69916	1.170009521	0.83584
IL-2	pg/uL	1.555284304	0.958652685	1.69916	1.170009521	0.83584
IL-4	pg/uL	2.70293953	1.469757606	3.066456874	1.589789961	0.73007
IL-5	pg/uL	2.733791358	0.483468636	2.294877709	0.532889145	0.20247
IL-6	pg/uL	23.69321154	5.870959318	25.5001467	3.740740655	0.57449
KC/Gro	pg/uL	33.572629	10.25454297	41.40277858	12.81035035	0.31105
TNFa	pg/uL	3.059163972	0.692809431	2.7762112	0.797750135	0.56262

Supplemental Table 4. Cytokine Analysis for Brain Regions

Brain Regions						
Hippocampus						
Parameter	**Units**	**FA Control Average**	**StDev**	**WFS Average**	**StDev**	**p-value**
IFNg	pg/uL	0.3181996	0.098363418	0.3069458	0.135608916	0.89644
IL-2	pg/uL	1.6787038	0.284619257	1.6107066	0.272781067	0.73902
IL-4	pg/uL	0.9880616	0.249356053	1.2249176	0.580647765	0.47494
IL-5	pg/uL	3.3160522	0.993926636	3.499909	1.692619196	0.85606
IL-6	pg/uL	26.335612	3.748252133	30.483802	15.88300545	0.62491
KC/Gro	pg/uL	8.404936	2.127606022	12.5786968	5.05167083	0.16629
IL-10	pg/uL	3.6744824	0.591343914	4.9162322	1.612889015	0.18628
IL-12/70p	pg/uL	38.843168	3.933849774	40.663074	9.840205371	0.7401
TNFa	pg/uL	0.78988625	0.127692061	0.754481667	0.198354711	0.81829
Prefrontal Cortex						
Parameter	**Units**	**FA Control Average**	**StDev**	**WFS Average**	**StDev**	**p-value**
IFNg	pg/uL	0.2472408	0.073927699	0.3646562	0.153603283	0.20564
IL-2	pg/uL	1.7687294	0.4386167	1.5588442	0.539872602	0.56291
IL-4	pg/uL	0.7447336	0.242376087	0.9436482	0.526143904	0.51165
IL-5	pg/uL	1.8154602	0.131277046	1.8355176	0.305502519	0.90695
IL-6	pg/uL	15.733548	2.78881225	15.075738	2.545249571	0.7365
KC/Gro	pg/uL	12.3446304	5.026649607	6.1758	0.923579048	0.04224
IL-10	pg/uL	5.3330868	1.432359302	4.8538306	1.270800909	0.63015
IL-12/70p	pg/uL	24.701376	6.096724444	26.44762	6.839413299	0.71299
TNFa	pg/uL	0.634205	0.099425835	0.7955274	0.077361326	0.0685

Supplemental Table 5. Cytokine Analysis from Bone Marrow

Bone Marrow						
Parameter	**Units**	**FA Control Average**	**StDev**	**WFS Average**	**StDev**	**p-value**
IL-9	pg/uL	25.39922247	3.843653901	27.12830721	4.999584051	0.42153
MCP-1	pg/uL	16.98219159	7.286451529	15.55154487	3.175196852	0.59582
IL-33	pg/uL	15.65391992	5.109649678	17.86981795	6.814107042	0.44523
IL-27/p28/IL-30	pg/uL	21.22084122	3.306444647	22.78251425	3.012411521	0.30877
IL-15	pg/uL	82.85468139	10.41580066	88.36704564	16.5629865	0.40909
IL-17A/F	pg/uL	5.431958264	0.733383083	6.019246217	1.374510865	0.27294
MIP-1a	pg/uL	111.5562294	21.23255208	127.0871616	29.59723504	0.2171
MIP-2	pg/uL	11.12986962	1.99878156	14.76132199	4.876218416	0.0534
IP-10	pg/uL	160.795755	46.63876241	218.2920846	57.88882817	0.03227
IFNg	pg/uL	1.525738118	0.221946435	1.549580419	0.251921647	0.83369
IL-10	pg/uL	3.513615759	0.479209669	3.424923945	0.737253373	0.76567
IL-12p70	pg/uL	35.83397093	5.992915738	33.5242705	7.808849531	0.49048
IL-1b	pg/uL	10.58945345	2.529348829	12.09768215	4.103281899	0.36032
IL-2	pg/uL	1.196612861	0.184977671	1.217193938	0.35474964	0.87907
IL-4	pg/uL	0.811593564	0.216012054	0.806939247	0.258491694	0.96739
IL-5	pg/uL	1.207813038	0.180266455	1.167593505	0.168198229	0.63048
IL-6	pg/uL	18.91239101	2.741409284	19.85401649	3.364350519	0.52332
KC/Gro	pg/uL	50.82090587	17.85871999	50.33665866	10.51032821	0.94488
TNFa	pg/uL	47.45198489	5.619448523	48.29691127	7.851765445	0.7959

Supplemental Data 6. Cardiac Function Data from Doppler Ultrasound Analysis

Parameter	Units	FA Control Average	StDev	WFS Average	StDev	t-test P-value
Heart Rate	BPM	503	45	475	67	0.25
Diameter;s	mm	3.2	0.28	3.2	0.29	0.99
Diameter;d	mm	4.16	0.23	4.2	0.23	0.7
Volume;s	µL	41.7	8.9	41.8	9.3	0.98
Volume;d	µL	77.4	9.9	79	10.3	0.7
Stroke Volume	µL	35.7	3.4	37.2	4	0.33
Ejection Fraction	%	46.8	5.5	47.8	5.7	0.66
Fractional Shortening	%	23.3	3.2	23.9	3.3	0.63
Cardiac Output	mL/min	18	2.9	17.8	3.6	0.86
LV Mass	mg	116.3	16	122	11.1	0.32
LV Mass Cor	mg	93	12.8	97.6	8.9	0.32
LVAW;s	mm	1.15	0.12	1.13	0.1	0.6
LVAW;d	mm	0.79	0.08	0.79	0.08	0.84
LVPW;s	mm	0.95	0.09	1.02	0.13	0.14
LVPW;d	mm	0.71	0.08	0.76	0.1	0.22